

# Lawrence Berkeley National Laboratory

## Recent Work

### Title

ISOBAR MODEL FIT TO THE REACTIONS  $N_n \rightarrow N_{nn}$  FITTING PROCEDURES AND FITS AT 1.7 BeV

### Permalink

<https://escholarship.org/uc/item/37d5r1vc>

### Author

Miller, Larry R.

### Publication Date

1971-11-01

2

ISOBAR MODEL FIT TO THE REACTION  $N\pi \rightarrow N\pi\pi$ :  
FITTING PROCEDURES AND FITS AT 1.7 BeV

Larry R. Miller  
(Ph. D. Thesis)

November 23, 1971

AEC Contract No. W-7405-eng-48

TWO-WEEK LOAN COPY

This is a Library Circulating Copy  
which may be borrowed for two weeks.  
For a personal retention copy, call  
Tech. Info. Division, Ext. 5545



2

## **DISCLAIMER**

This document was prepared as an account of work sponsored by the United States Government. While this document is believed to contain correct information, neither the United States Government nor any agency thereof, nor the Regents of the University of California, nor any of their employees, makes any warranty, express or implied, or assumes any legal responsibility for the accuracy, completeness, or usefulness of any information, apparatus, product, or process disclosed, or represents that its use would not infringe privately owned rights. Reference herein to any specific commercial product, process, or service by its trade name, trademark, manufacturer, or otherwise, does not necessarily constitute or imply its endorsement, recommendation, or favoring by the United States Government or any agency thereof, or the Regents of the University of California. The views and opinions of authors expressed herein do not necessarily state or reflect those of the United States Government or any agency thereof or the Regents of the University of California.

ISOBAR MODEL FIT TO THE REACTION  $N\pi \rightarrow N\pi\pi$ :  
FITTING PROCEDURES AND FITS AT 1.7 BEV. \*

Larry R. Miller  
Lawrence Berkeley Laboratory  
University of California  
Berkeley, California

November 23, 1971

ABSTRACT

The Isobar Model has been fit to 50,000 events of the reaction  $N\pi \rightarrow N\pi\pi$  in the energy region 1640 to 1800 Mev. Sixty combinations of partial waves and intermediate resonances were considered. The data were divided into six energy bins and independent fits were done to the model in each bin. The method of maximum likelihood was used, and at each energy no further binning or projecting was necessary.

A solution has been found that represents the data well by several criteria and is continuous among the six energy bins. This solution is stable and perhaps unique but it is surprising; instead of finding resonance-like phase changes in the production amplitudes of waves that pass through resonance in the elastic channel, we find that virtually none of the production amplitudes change in phase (with respect to each other at least) over the whole energy region.

---

\* This work was supported by a Hughes Aircraft Company Doctoral Fellowship and by the U.S. Atomic Energy Commission.

## I. INTRODUCTION

The Isobar Model was proposed by Lindenbaum and Sternheimer<sup>1</sup> in 1957 after it was found that the reaction  $N\pi \rightarrow N\pi\pi$  favors final states in which the mass of a  $N\pi$  subsystem is near 1236 Mev., the mass of the P33  $N\pi$  resonance. Their Isobar Model postulated that this resonance and a separate  $\pi$  were first formed and that the resonance then decayed into a N and the other  $\pi$ . This decay was assumed to take place outside the spatial region of the formation.

Our Isobar Model is generalized to include several resonances. The amplitude for a reaction such as  $N\pi \rightarrow N\pi\pi$  is written as the sum of several individual amplitudes, each of which is the product of two parts: the first part is an amplitude to form from a particular incoming partial wave an intermediate state consisting of a stable particle and a resonance, and the second part is the amplitude for the resonance to decay into the other two final particles.

This paper describes a fit of the Isobar Model to the reaction  $N\pi \rightarrow N\pi\pi$  in the center-of-mass-energy region between 1640 and 1800 MeV. Three final-state resonances are considered: the  $\Delta(1236)$   $N\pi$  ( $L=1, I=\frac{3}{2}, J=\frac{3}{2}$ ) resonance, the  $\rho(760)$  ( $L=1, I=1, J=1$ )  $\pi\pi$  resonance, and the  $\sigma(800)$  ( $L=0, I=0, J=0$ )  $\pi\pi$  enhancement. The decay amplitudes of these resonances are taken as fixed quantities. The production amplitudes for the intermediate state are the variable quantities to be determined by the fitting procedure (see Fig. 1 below).

Our data consist of 50,000 events of the types

$$\begin{array}{l} p\pi^- \rightarrow n\pi^-\pi^+ \\ p\pi^- \rightarrow p\pi^-\pi^0 \\ p\pi^+ \rightarrow p\pi^+\pi^0 \end{array}$$

The sources of the data are discussed in section IV. The energy region 1640 to 1800 MeV is divided into six bins. Separate fits are done to events in each of these bins. With about 10,000 events in each energy bin we find reasonable fits. Continuity of solutions from one energy to the next is looked for after the fits for each bin are done. Fitting separately at each energy avoids the necessity of making a priori assumptions about the energy dependence of the fitted production amplitudes. The maximum-likelihood fitting method is used with no binning or projecting in the other kinematic variables. The event population of each bin is given in Fig. 5. The bins are labeled by their central energy values.

## II. THE ISOBAR MODEL

The following quantum numbers, along with the quantum numbers of the five individual particles form a complete set for the description of the reaction  $N\pi \rightarrow N\pi\pi$ .

- P Momentum of the incoming nucleon in the center-of-mass.
- I Total isospin.
- J Total spin.
- $\lambda$  z-component of total spin.
- Q Momentum of particle 3 in the center-of-mass.
- L' Orbital angular momentum between particle 3 and pair 12.
- q Momentum of particle 1 in the center-of-mass of the 1,2 system.
- $\ell$  Orbital angular momentum of the 1,2 system.
- j Total spin of the 1,2 system. If the nucleon is in the 1,2 system, j is  $\ell$  combined with the nucleon spin. If the nucleon is particle 3, then  $j = \ell$ .
- $\lambda_j$  Helicity of the 1,2 system in the overall center-of-mass. This is the projection of j along the direction of the momentum of the 1,2 system in the overall center-of-mass.
- S 'Total spin of the final state'.  $S(S+1)$  is the eigenvalue of the operator  $\hat{S} = \hat{J} + \hat{s}$ .  $\hat{J}$  measures the total spin of the 1,2 system, and  $\hat{s}$  measures the spin of particle 3. J is S combined with L' ( $\hat{J} = \hat{S} + \hat{L}'$ ).
- $\mu_A$  Helicity of the incoming nucleon.
- $\mu_B$  Helicity of the outgoing nucleon.

These quantum numbers may be displayed symbolically:

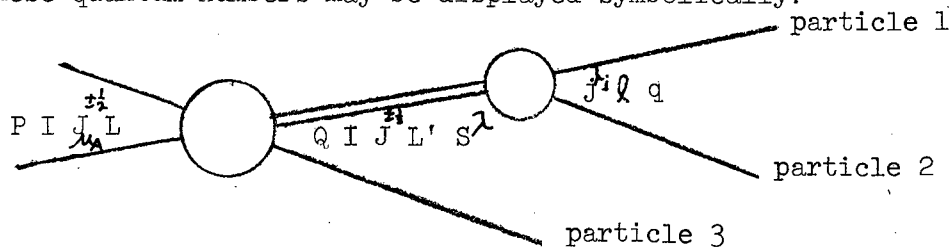


Fig. 1. Quantum Numbers.

For a given  $J$  and  $L'$ ,  $L$  may take on two values since the nucleon spin is combined with  $L$  to form  $J$ , e.g.  $SS_{\frac{1}{2}}$  and  $PS_{\frac{1}{2}}$ . Parity conservation always allows just one of these two combinations.

Let the variable  $\kappa$  index the set  $(I, J, L', j, l)$ . Then the most general matrix element for the reaction  $N\pi \rightarrow N\pi\pi$  may be written:

$$M_{\mu_A \mu_B}^{\mu} = \sum_{\kappa} T_{\kappa}(P, Q, q) \langle \kappa^{\mu} A^{\mu_B} | P_1 P_2 P_3 \rangle \quad (1)$$

The  $T$  are arbitrary complex numbers. (The quantum numbers of the waves we consider are given in Fig. 2. For these,  $\kappa$  takes on ten values, the length of the longest column.)

The most important resonance bands covered by a  $N\pi\pi$  Dalitz plot, e.g. Fig. 9, with total mass less than 1800 MeV are two different  $\pi\pi$  resonances,  $\sigma(j=1=0)$  and  $\rho(j=1=1)$ , and two different charge states of the  $\Delta(j=\frac{3}{2}, l=1) N\pi$  resonance.

For a particular resonance in a particular diparticle, the Isobar Model restricts  $T_{\kappa}(P, Q, q)$  to have the form

$$T_{\kappa}(P, Q, q) = \begin{cases} A_{\kappa}(P) B(q) Q^{L'} & \text{if } j \text{ and } l(\text{in } \kappa) \text{ are the} \\ & \text{quantum numbers of the} \\ & \text{resonance.} \\ 0 & \text{otherwise} \end{cases} \quad (2)$$

$A_{\kappa}(P)$  is an arbitrary complex function of the center-of-mass energy, and  $B(q)$  is the decay amplitude of the resonance, and  $Q^{L'}$  is the centrifugal barrier penetration factor for the production amplitude.



Our total matrix element  $M_{\mu_A \mu_B}^{\text{total}}$  is the sum of four matrix elements, one for the  $\sigma$ , one for the  $\rho$ , and one for each of the two  $N\pi$  diparticles that may form a  $\Delta$  resonance:

$$M_{\mu_A \mu_B}^{\text{total}} = M_{\mu_A \mu_B}^{\rho} + M_{\mu_A \mu_B}^{\sigma} + M_{\mu_A \mu_B}^{\Delta_1} + M_{\mu_A \mu_B}^{\Delta_2} . \quad (3)$$

Each of the four elements on the right is given by Eqs. 1 and 2 using the indicated resonance and decomposition. The index  $k$  will index over the three resonances and also over the set indexed by  $\mathcal{K}$  (so for Table 1,  $k=1, \dots, 60$ ). An arbitrary complex function  $A_k(P)$  exists for each  $k$ . These are the production amplitudes to be determined by the fits. Within each of the six energy bins, the  $A_k(P)$  are assumed constant. These constant  $A_k$  are the free parameters of the likelihood maximizing procedure.

We have no polarization information on our events. Our predicted differential cross section (or likelihood) for an event is proportional to the sum over helicities of the absolute square of the total matrix element, i.e.  $d\sigma(\text{pred.})/dt \cong p$ ,

$$p_{\mathcal{A}}^c(w_i^c) \cong p^c(w_i^c) = \sum_{\mu=1}^4 \left| \sum_{k=1}^{n_k} A_k X_{k\mu}^c(w_i^c) \right|^2 . \quad (4)$$

Several new symbols have been defined:

- c      The charge channel. There are five charge channels for the reaction  $N\pi \rightarrow N\pi\pi$ . We use data from three, but the model will predict differential cross sections for all five channels.
- $w, w_i^c$        $w$  stands for the kinematic variables of an event.  $w_i^c$  indicates the kinematic variables of the  $i$ -th event in channel  $c$ .
- $\mu$       The values 1 thru 4 of  $\mu$  correspond to the four combinations of helicities  $\mu_A = \pm 1/2, \mu_B = \pm 1/2$ .
- $p$       The differential cross section predicted by the model.

- $n_k$  The number of 'waves'. The number of combinations of discrete quantum numbers and resonances.
- $\underline{A}$  A vector of dimension  $2n_k$  corresponding to the set of complex numbers  $A_k$ :  $\underline{A} = (\text{Re}A_1, \text{Im}A_1, \text{Re}A_2, \text{Im}A_2, \dots)$ .
- $X_{k\mu}^c$  Complex functions of the kinematic variables of an event. These numbers are obtained by combining Eqs. 1, 2, and 3, and equating the result to Eq. 4. These are constants supplied to the fitting procedure.

A 'wave' (or value of  $k$ ) is specified by giving the resonance and by the quantum numbers  $L', I, J$ , and  $L$  ( $L$  is redundant but useful). The latter numbers will be displayed using the convention  $(L)(L')(2I)(2J)$ , with  $L$  and  $L'$  given in spectroscopic notation, i. e. S, P, D, F,.... With the  $\rho$  resonance, the quantum number  $S$  is also required since in this case, it may take on two values.  $2S$  will be subscripted to the symbol  $\rho$ .

We consider sixty different possible 'waves'. The combinations of quantum numbers and resonances making up these waves are as follows.

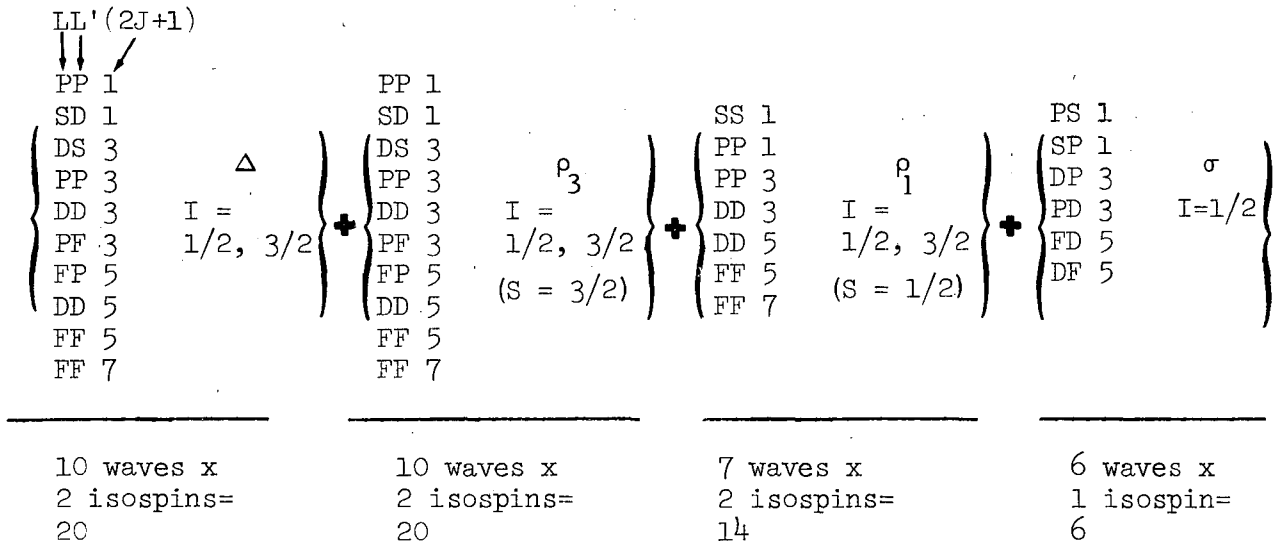


Fig. 2. The Sixty-Wave Set.

III. FITTING PROCEDURES

A. The Maximum Likelihood Formulation

In our experiment, we must 'normalize' the data to three different known channel cross sections. This is done as follows using the Poisson probability density.

For a given set of production amplitudes  $A_k$ , the likelihood that the  $N^c$  events  $\{w_1^c, w_2^c, \dots, w_{N^c}^c\}$  will occur in charge channel  $c$  is denoted by

$$\mathcal{L}^c = \rho(\{w_1^c, w_2^c, \dots, w_{N^c}^c\} | (A_1, A_2, \dots, A_{n_k})). \quad (5)$$

Defining the normalization of  $\rho^c$  in Eq. 4,

$$R^c \equiv \int_{\substack{\text{phase-space} \\ \text{(at fixed energy)}}} p^c(w) d^4w,$$

the likelihood is the Poisson probability

$$\mathcal{L}^c = e^{-\frac{R^c N^c}{\sigma^c}} \prod_{i=1}^{N^c} p^c(w_i^c). \quad (6)$$

This equation is obtained from Eq. 36 of Ref. 2 by observing that if the number of events per microbarn for the experiment is  $\ell^c$ , then the actual number of events in the experiment is  $N^c = \ell^c \sigma^c$  and the predicted number is  $\nu = \ell^c R^c$ .

$p^c$  and  $R^c$  may be scaled simultaneously by changing the magnitudes of all  $A_k$  by the same scale factor.  $\mathcal{L}^c$  may be immediately maximized in this degree of freedom. We now show that the maximum occurs when  $R^c = \sigma^c$ .

To see this, we write the derivative of  $\mathcal{L}^c$  with respect to the scale factor  $s$ .

$$\mathcal{L}^c(sA) = s^{2N^c} e^{-\frac{s^2 R_A^c N^c}{\sigma^c}} \prod_{i=1}^{N^c} p_A^c(w_i^c).$$

$$\frac{\partial \mathcal{L}^c(sA)}{\partial s} = 2s \left( \frac{N^c}{s^2} - \frac{R_A^c N^c}{\sigma^c} \right) \mathcal{L}^c(A).$$

Setting this to zero gives  $s^2 = \frac{\sigma^c}{R_A^c}$ , so  $R_{sA}^c = s^2 R_A^c = \sigma^c$ .

The likelihood for more than one channel is the product of the likelihoods for each channel.

$$\mathcal{L} = \prod_c \mathcal{L}^c = \prod_c \left[ e^{-\frac{R^c N^c}{\sigma^c}} \prod_{i=1}^{N^c} \frac{p^c(w_i^c)}{\sigma^c} \right].$$

The logarithm of  $\mathcal{L}$  is

$$\log \mathcal{L} = \sum_c \log \mathcal{L}^c = \sum_c \left[ -\frac{R^c N^c}{\sigma^c} + \sum_{i=1}^{N^c} \log p^c(w_i^c) \right] +$$

+ terms constant in A.

In general, it is not possible to adjust the complex numbers  $A_k$  so that  $R^c$  will equal  $\sigma^c$  for all  $c$ . The likelihood increases, however, when this is nearly true. The likelihood favors cases where the cross section for each channel is predicted accurately. The numbers of events used in each channel need not be proportional to the cross section in the channel.

For use in the fitting procedure, a function  $\bar{J}$  is defined.

$\bar{J}$  is an 'average log likelihood':

$$\bar{J}(A) \equiv \frac{1}{N} \log (\max_s \mathcal{L}(sA) ).$$

$\bar{J}$  is obtained from an  $\mathcal{L}$  which has been pre-maximized with respect to the scale factor.  $\bar{J}$  is then invariant to change in scale of the A.

This maximization is done by finding an  $s^{\max}$  such that

$$\left. \frac{\partial \log \mathcal{L}(sA)}{\partial s} \right|_{s=s^{\max}} = 0.$$

This  $s^{\max}$  is then substituted back to get  $\bar{J}(A) = \frac{1}{N} \log \mathcal{L}(s^{\max} A)$ .

Explicitly,  $p_{sA}^c(w) = s^2 p_A^c(w)$  and  $R^c(sA) = s^2 R^c(A)$  so

$$\frac{1}{N} \log \mathcal{L}(sA) = \frac{1}{N} \sum_c \left[ -\frac{s^2 R^c N^c}{\sigma^c} + \sum_{i=1}^{N^c} (\log p^c(w_i^c) + \log s^2) \right].$$

$$\frac{\partial}{\partial s} \frac{1}{N} \log \mathcal{L}(sA) = \frac{2s}{N} \sum_c \left[ -\frac{R^c N^c}{\sigma^c} + \frac{N^c}{s} \right].$$

Equating this derivative to zero gives

$$s^{\max} = \frac{N}{\sum_c \frac{R^c N^c}{\sigma^c}}.$$

Substituting  $s^{\max}$  back,

$$\mathcal{F}(A) = \frac{1}{N} \log \mathcal{L}(s^{\max A}) = \frac{1}{N} \sum_c \left[ \sum_{i=1}^{N^c} \log p^c(w_i^c) \right] - \log \sum_c \frac{R^c N^c}{\sigma^c} +$$

+ terms constant in A. (7)

In these equations,  $N \equiv \sum_c N^c$ .

Use of this 'average' log likelihood aids in comparing likelihoods between runs with different numbers of events.

## B. Numerical Techniques

### 1. Introduction

The fitting procedure consists of finding sets A that correspond to maxima of  $\mathcal{F}(A)$ . Starting values for A are chosen at random and varied in steps. The value of A at each step is an estimate of the position of the maximum. This estimate is based on information obtained at previous steps. At each step, the values of  $\mathcal{F}$ , its first derivatives, and possibly its second derivatives are calculated. If the first derivatives are not zero, the next estimate of the local maximum is based on this and previous information. The next step will be at this new estimate.

Maximizing procedures fall generally into three categories: those that evaluate only the function at each step, those that evaluate at each step the function and its first-derivative vector, and those that evaluate at each step the function, its first-derivative vector, and its second-derivative matrix. We have found that the most efficient technique is a combination of the latter two types. We use the Davidon<sup>3</sup> method, which is of the second type, and a modified form of the Newton-

Raphson method<sup>4</sup>, which is of the third type.

In both the Davidon and Newton-Raphson methods, the change made in  $\underline{A}$  to obtain the new estimate,  $\Delta \underline{A}$ , is the negative of the product of a matrix called the variance matrix and the first-derivative vector at the last step:  $\Delta \underline{A} = -\nabla \mathcal{J}(\underline{A}_i) \mathcal{J}(\underline{A}_i)^{-1}$ . The variance matrix approximates the curvature of the space. If a) the function  $\mathcal{J}(\underline{A})$  is quadratic in the components of  $\underline{A}$ , and b) the variance matrix is truly the inverse of the second-derivative matrix, then the maximum will be reached on the second step.

## 2. The Davidon Method

In the Davidon method, a diagonal guess is used as the variance matrix for the first step. At each subsequent step, this matrix is adjusted by adding a rank-one matrix. A rank-one matrix is a matrix having just one eigenvector with non-zero eigenvalue. A typical example is the outer product of a vector  $\underline{v}$  with itself:  $M_{ij} = v_i v_j$  or equivalently  $M = \underline{v} \underline{v}^T$ . The superscript  $T$  means 'transpose'. A matrix of the form of  $M$  is called a 'projector'. The Davidon variance matrix  $V_i$  at step  $i$  is adjusted by adding a projector multiplied by a number:

$$V_{i+1} = V_i + \lambda (V_i \nabla \mathcal{J}_i)(V_i \nabla \mathcal{J}_i)^T$$

The number  $\lambda$  is calculated from the current variance matrix  $V_i$  and from the derivative vectors at the current and previous step,  $\nabla \mathcal{J}_i$  and  $\nabla \mathcal{J}_{i-1}$ . The adjustment to the variance matrix reflects the additional knowledge about the curvature of the space gained from knowing the new first-derivative vector. To insure that the process will tend to a maximum rather than to a minimum or saddle-point,  $\lambda$

is modified if necessary to keep the new variance matrix negative-definite. If the  $2n_k$ -dimensional  $\underline{A}$  space is quadratic, then after  $2n_k$  steps the variance matrix will exactly correspond to the curvature of the space. The next step will then be at the maximum.

### 3. The Modified Newton-Raphson Method

The Newton-Raphson method recalculates the variance matrix afresh at each step. The modified version which we use calculates a negative-definite approximation to the local second-derivative matrix. This approximation is inverted to obtain the variance matrix. The approximation is such that if the events are distributed nearly as the model predicts for a vector  $\underline{A}$ , then the approximate matrix is nearly equal to the local second-derivative matrix at  $\underline{A}$ . The following paragraphs discuss the form of this matrix.

The  $2n_k$ -dimensional real first-derivative vector of  $\mathcal{F}$  (of Eq. 7) is

$$\nabla \mathcal{F}(\underline{A}) = \frac{1}{N} \sum_c \sum_{i=1}^{N^c} \frac{\nabla p^c(w_i^c)}{p^c(w_i^c)} - \frac{\sum_c \frac{\nabla R^c N^c}{\sigma^c}}{\sum_c \frac{R^c N^c}{\sigma^c}} \quad (8)$$

The  $2n_k$  by  $2n_k$  real second-derivative matrix of  $\mathcal{F}$  is

$$\begin{aligned} \nabla \nabla^T \mathcal{F}(\underline{A}) &= \frac{1}{N} \sum_c \sum_{i=1}^{N^c} \left[ \frac{\nabla \nabla^T p^c(w_i^c)}{p^c(w_i^c)} - \frac{(\nabla p^c(w_i^c)) (\nabla p^c(w_i^c))^T}{p^c(w_i^c)^2} \right] \\ &- \frac{\sum_c \frac{N^c}{\sigma^c} \nabla \nabla^T R^c}{\sum_c \frac{R^c N^c}{\sigma^c}} + \frac{\left( \sum_c \frac{N^c \nabla R^c}{\sigma^c} \right) \left( \sum_c \frac{N^c \nabla R^c}{\sigma^c} \right)^T}{\left( \sum_c \frac{R^c N^c}{\sigma^c} \right)^2} \\ &\equiv M_1 + M_2 + M_3 + M_4 \quad (9) \end{aligned}$$



If the function  $p^c(w)$  closely approximates the distribution of events then  $R^c \approx \sigma^c$  and the sum over events of any function may be to good approximation replaced by the phase-space integral of the function multiplied by  $p^c(w)$ . Thus

$$\begin{aligned} M_1 &= \frac{1}{N} \sum_c \sum_{i=1}^{N^c} \frac{\nabla \nabla^T p^c(w_i^c)}{p^c(w_i^c)} \approx \\ &\approx \sum_c \frac{N^c}{N} \int_{\text{phase-space}} \frac{\nabla \nabla^T p^c(w)}{p^c(w)} p^c(w) d^4 w = \\ &= \sum_c \nabla \nabla^T \int_{\text{phase-space}} p^c(w) d^4 w \frac{N^c}{N} = \sum_c \frac{N^c}{N} \nabla \nabla^T R^c. \end{aligned}$$

Then to the above two approximations,  $M_1$  and  $M_3$  cancel:  $M_1 + M_3 = 0$ .

From Eq. 4 the first-derivative vector of  $p^c(w)$  may be found.

$$\frac{\partial}{\partial \begin{pmatrix} \text{Re} \\ \text{Im} \end{pmatrix} A_k} p^c(w) = \begin{pmatrix} \text{Re} \\ \text{Im} \end{pmatrix} \sum_{\mu=1}^4 2X_{k\mu}^{c*} \left( \sum_{k'=1}^{n_k} A_{k'} X_{k'\mu}^c(w) \right) \quad (10)$$

This leads to the interesting result

$$\underline{A}^T \nabla p^c(w) = 2p^c(w) .$$

and consequently

$$\underline{A}^T \nabla R^c = 2R^c .$$

These two relations may be used to show that  $\underline{A}$  is a null vector (approximately) of  $\nabla \nabla^T \mathcal{J}$ :

$$\begin{aligned}
 (\nabla \nabla^T \mathcal{J})_{\underline{A}} &\approx M_2 \underline{A} + M_4 \underline{A} = -\frac{2}{N} \sum_c \sum_{i=1}^{N^c} \frac{\nabla p^c(w_i^c)}{p^c(w_i^c)} + 2 \frac{\sum_c \frac{N^c \nabla R^c}{\sigma^c}}{\sum_c \frac{R^c N^c}{\sigma^c}} \\
 &\approx \left( -\frac{2}{N} + \frac{2}{\sum_c \frac{R^c N^c}{\sigma^c}} \right) \cdot \sum_c \nabla R^c \approx 0.
 \end{aligned}$$

As before the assumption  $R^c \approx \sigma^c$  is made.)

We can verify the above observation with the general observation that at a local maximum,  $\underline{A}$  is an exact null vector of  $\nabla \nabla^T \mathcal{J}$  because of the scale-invariance of  $\mathcal{J}$ . Scale invariance implies that  $(\nabla^T \mathcal{J})_{\underline{A}} = 0$ , since  $\underline{A}$  itself is the generator for scale changes of  $\underline{A}$ . Differentiating again,  $(\nabla \nabla^T \mathcal{J})_{\underline{A}} + (\nabla^T \mathcal{J})_{\underline{I}} = 0$ , where  $\underline{I}$  is the identity matrix. Thus  $(\nabla \nabla^T \mathcal{J})_{\underline{A}} = -\nabla^T \mathcal{J} = 0$ .

$\mathcal{J}(\underline{A})$  is also invariant to a simultaneous change in phase of all  $A_k$ . The vector  $\underline{(iA)} \equiv (\text{Im}A_1, -\text{Re}A_1, \dots, \text{Im}A_{n_k}, -\text{Re}A_{n_k})$ , which generates phase changes in  $A$  is also a null vector of  $\nabla \nabla^T \mathcal{J}$  at a local maximum for the same reason. These singularities, which are due to redundant parameterization, are commonly eliminated in fitting problems similar to ours by permanently freezing one phase and one amplitude in the  $A_k$  and reducing the dimension of the second-derivative matrix by two.

We find, however, that the maximizing procedure takes less than one-third the number of steps to reach a maximum if all the  $A_k$  are permitted to vary. A proper variance matrix is obtained from our nearly-singular second-derivative matrix  $\nabla \nabla^T \mathcal{J}$  as follows.

The second-derivative matrix may be decomposed spectrally as

$$\nabla\nabla^T J = \sum_{l=1}^{2n_k} \lambda_l \underline{v}_l \underline{v}_l^T \quad \text{where } \underline{v}_l^T \underline{v}_{l'} = \delta_{ll'}. \quad \underline{v}_l \text{ are the eigenvectors and}$$

$\lambda_l$  are their eigenvalues. Writing the two near-zero eigenvalues separately,

$$\nabla\nabla^T J = \sum_{l=3}^{2n_k} \lambda_l \underline{v}_l \underline{v}_l^T + \lambda_1 \frac{\underline{A}\underline{A}^T}{|\underline{A}|^2} + \lambda_2 \frac{(\underline{iA})(\underline{iA})^T}{|\underline{A}|^2}, \quad (11)$$

$$\lambda_1, \lambda_2 \approx 0.$$

The desired variance matrix is the inverse of  $\nabla\nabla^T J$  restricted to the space of vectors orthogonal to both  $\underline{A}$  and  $(\underline{iA})$ :

$$V = \sum_{l=3}^{2n_k} \frac{1}{\lambda_l} \underline{v}_l \underline{v}_l^T. \quad (12)$$

To obtain this V, a matrix M is first calculated:

$$M \equiv \nabla\nabla^T J - (M_1 + M_3) - \frac{(\underline{iA})(\underline{iA})}{|\underline{A}|^2} - M_4. \quad (13)$$

$M_4$  (see Eq. 6) is the projector for the vector

$$\frac{\sum_{c=1}^{N^c} \frac{N^c \nabla R^c}{\sigma^c}}{\sum_{c=1}^{N^c} \frac{N^c R^c}{\sigma^c}}$$

Since  $\underline{A}^T \nabla R^c = 2R^c$ , this vector has a large component along  $\underline{A}$ .

Subtraction of this projector changes the eigenvalue of  $\underline{A}$  from nearly zero to the substantial negative number  $-4 + \lambda_2 \approx -4$ . Subtraction of

the projector  $\frac{(\underline{iA})(\underline{iA})}{|\underline{A}|^2}$  changes to  $-1 + \lambda_1 \approx -1$ . The sum

$(M_2 + M_3)$  is approximately zero and is subtracted to simplify the

expression to be evaluated by the computer (and also as will be seen

to ensure that the variance matrix is negative-definite). Eqs. 9, 11,

and 13 give

$$M \equiv -\frac{1}{N} \sum_c \sum_{i=1}^{N^c} \frac{(\nabla p^c(w_i^c))(\nabla p^c(w_i^c))^T}{p^c(w_i^c)^2} - \frac{(\underline{iA})(\underline{iA})^T}{|\underline{A}|^2} \quad (14)$$

For this M,

$$M \underline{\underline{A}} \approx \frac{1}{4} \underline{\underline{A}} \quad \text{and} \quad M \underline{\underline{(iA)}} \approx \underline{\underline{(iA)}}.$$

This M is the negative of a sum of projectors so its eigenvalues must all be non-positive. If the model does not have special degeneracies and if there are more than  $2n_k - 2$  events, as in our case, then M has no zero eigenvalues and is therefore negative-definite.

M is inverted and  $\frac{\underline{\underline{(iA)}(iA)^T}}{|A|^2} + \frac{\frac{1}{4} \underline{\underline{A}} \underline{\underline{A}}^T}{|A|^2}$  is added to the result to obtain V:

$$V = M^{-1} + \frac{\underline{\underline{(iA)}(iA)^T}}{|A|^2} + \frac{\frac{1}{4} \underline{\underline{A}} \underline{\underline{A}}^T}{|A|^2}.$$

Since  $M^{-1} \underline{\underline{A}} \approx \frac{1}{4} \underline{\underline{A}}$  and  $M^{-1} \underline{\underline{(iA)}} \approx \underline{\underline{(iA)}}$ ,  $\underline{\underline{A}}$  and  $\underline{\underline{(iA)}}$  are nearly null vectors of V as desired (see Eq. 12). This V is the variance matrix for the Newton-Raphson procedure.

The inverse of M is computed using the 'square root method' for inverting symmetric positive-definite (or negative-definite) matrices<sup>5</sup>. The computer time for inversion varies as the cube of  $n_k$  and is 0.3 seconds for  $n_k=30$ .

#### 4. The Error Matrix

The error matrix is closely related to V of Eq. 11. At a local maximum, the error matrix  $E \equiv \langle \delta A \delta A^T \rangle$  is  $\frac{1}{N} V$  (see Eq. 14 of Ref. 2). The factor  $\frac{1}{N}$  arises from our use of  $\bar{F}$ , the 'average' log likelihood.

In the neighborhood of a local maximum  $\mathcal{L}^{\max}$ , in the quadratic approximation, the hypersurface on which the likelihood is  $\frac{\mathcal{L}^{\max}}{\sqrt{e}}$  is a hyper-ellipse called the error ellipse. It is centered at the

maximum. The maximum extent of the error ellipse along any coordinate axis  $i$  is the square root of the error-matrix element  $E_{ii}$ . Fig. 3a gives a two-dimensional projection of the error ellipse on the  $\tilde{A}_i - \tilde{A}_j$ -plane about a local maximum  $\mathcal{L}^{\max} \equiv \mathcal{L}(\tilde{A}^{\max})$ .  $\tilde{A}_i$  and  $\tilde{A}_j$  are any two of the  $2n_k$  coordinates. This two-dimensional ellipse outlines the maximum extent of the error ellipse projected on the  $\tilde{A}_i - \tilde{A}_j$ -plane as all other components of  $A$  are varied. It is the set of points  $(x, y)$  for which

$$\max_{\substack{\text{varying all} \\ \tilde{A}_k \text{ where } k \neq i, j \\ \text{and with } \tilde{A}_i = x \\ \text{and } \tilde{A}_j = y.}} \mathcal{L}(\tilde{A}) = \frac{\mathcal{L}^{\max}}{\sqrt{e}}$$

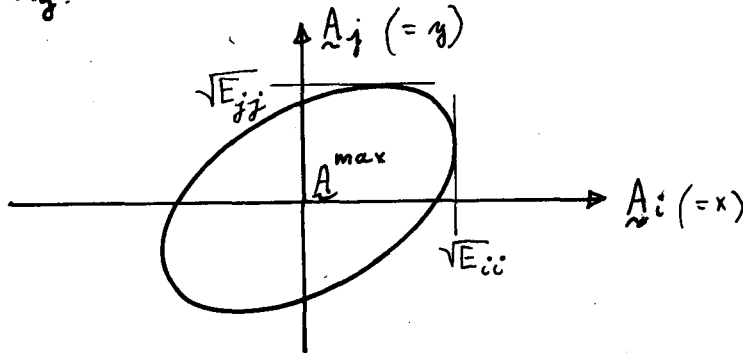


Fig. 3a. Two-Dimensional Projection of the Error Ellipse

If, in particular,  $i$  and  $j$  are taken to correspond to the real and imaginary parts respectively of a single  $A_k$ , then this two-dimensional ellipse encloses the probable region of the complex number  $A_k$  in the following sense. If  $A_k$  is constrained to occupy another (complex) point within the two-dimensional ellipse and all other  $A_k$ , are varied to re-maximize the likelihood, then the likelihood will be lower than  $\mathcal{L}^{\max}$  by a factor between  $\frac{1}{\sqrt{e}}$  and one.

The results presented in the next section will include 'error bars'

which represent these two-dimensional real-imaginary error ellipses for each  $A_k$ . The error bars for an  $A_k$  are the major and minor axes of an ellipse twice the size of the two-dimensional error ellipse for  $A_k$ .

#### 5. Our Combination of the Newton-Raphson and Davidon Methods

Using thirty waves, the calculation of the second-derivative matrix takes roughly four times as long as the calculation of both the function  $\mathcal{F}$  and its first-derivative vector. If a few hundred or more events are used, then the matrix inversion time is much smaller than either of these times. The Newton-Raphson step therefore takes five times as long as the Davidon step (in this paper, a Newton-Raphson step indicates the set of  $A_k$  for which a new Newton-Raphson variance matrix is calculated; the step following a Newton-Raphson step is the first to make use of the new Newton-Raphson variance matrix). If the curvature changes much from point to point in the stepping procedure, then the variance matrix will always be somewhat out of date. We find it best to renew the accuracy of the variance matrix periodically by taking Newton-Raphson steps. The matrix obtained from a Newton-Raphson step is retained and updated by subsequent Davidon steps. The efficiency of steps (change in per step) is high for several steps after a Newton-Raphson step. Fig. 5 plots the increase in  $\mathcal{F}$  per step against the step number for a typical fit. The dots indicate Davidon steps and the circles indicate Newton-Raphson steps (calculations). The first dot after the circle is the change in  $\mathcal{F}$  for the first step that makes use of the new Newton-Raphson variance matrix!

All the fits we have done have the same general behavior as that in

Fig. 5. The step size diminishes rapidly from the first to about the tenth step. The step size for the next forty to eighty steps decreases very slowly. During these steps the likelihood increases roughly linearly and the  $A$  change radically. The  $A_k$  weave among each other singly or in small groups (such as DS13 and DD13 together) in a complicated pattern. By the end of these forty to eighty steps, the rough nature of the eventual solution is established.

Finally forty to eighty additional steps are taken. The step size diminishes rapidly during these steps and the solution shifts by three or four standard deviations. The convergence during these last steps is quadratic: the change in  $\mathcal{J}$  at each step is roughly a constant multiplied by the square of the change at the previous step. The dashed line in Fig. 5 indicated quadratic behavior for a constant of fifty, i.e. where  $\mathcal{J}_i - \mathcal{J}_{i-1} \approx 50 (\mathcal{J}_{i-1} - \mathcal{J}_{i-2})^2$ . Quadratic convergence is expected for smooth functions such as ours when using a fitting method that explicitly calculates the variance matrix.

We terminate the fitting when the magnitude of the change in  $A$  per step is less than  $10^{-4} |\underline{A}|$  for four successive steps. This occurred at step 122 for the fit of Fig. 5. The change of  $\underline{A}$  per step is so small at this point that  $\underline{A}$  could change by only a fraction of a standard deviation in hundreds of additional steps. In fact, the change in  $\underline{A}$  will go to  $10^{-14} |\underline{A}|$  if the fit is allowed to continue for twenty or thirty more steps.

Fig. 5 indicates that adopting even a much less strict criterion for stopping cannot save many steps. The  $A_k$  are roughly one standard deviation away from their final values at step 100 on this figure.

Fig. 6 plots the difference between the current value of  $\mathcal{F}$  and its value at the maximum against execution time on the CDC 6600 computer. Several combinations of Davidon and Newton-Raphson methods are shown. A combination of the two methods is superior to either method alone.

Fig. 7 indicates the shape of the log-likelihood space in the neighborhood of a maximum as two of the  $2n_k$  variables are varied. We have made about thirty such two-dimensional slices with various pairs of variables and the results in all cases were qualitatively similar to this.

### C. A Test Of The Fitting Procedure

From preliminary fits to our data, we have found a set of thirty-four waves that approximate the event distribution fairly well. This set of waves and amplitudes was used to test the maximum-likelihood fitting procedure. An artificial set of 6300 fake events was created by generating events with a frequency proportional to  $p_A^c(w) \times d(\text{phase space})$ . The fitting procedure was then applied to these events as follows.

Ten thousand random 'starting vectors'  $A$  were generated, and we then kept the five of these sets having the highest likelihood for the 6300 fake events. A separate sixty-wave fit was done to maximize the likelihood starting with each of these five sets. Four of the five fits reached the same maximum. This maximum was within errors of the generating set  $A$  (both for the 34 non-zero  $A_k$  and also for the 26 zero waves). The fifth fit resulted in a totally different maximum.

Finally, a 34-wave fit was done using those 34 waves with which



the artificial events were generated. The resulting amplitudes agreed well with the generating amplitudes. The value of  $\bar{f}$  at the maximum was 0.275.

#### IV. RESULTS

##### A. The Data

We use  $\pi^-p$  data from two experiments: an exposure at Berkeley in the 72-inch hydrogen bubble chamber, and one at Argonne National Laboratory in the 30-inch MURA hydrogen bubble chamber. The Berkeley exposure consists of 200,000 pictures taken at 9 momenta between 900 and 1200 Mev./c. This data was taken for an earlier experiment and is described in Ref. 6.

The Argonne exposure was made in 1967 and consists of 500,000 pictures taken at 26 momenta between 550 Mev./c and 1600 Mev./c. Ref. 7 describes this data.

The  $p\pi^+$  data comes from Saclay where film from several laboratories was analyzed. This data includes 10,000 events in the 1600 to 1800 Mev. region. The data is described in Ref. 8.

##### B. The Solution

At each of the six energies, fits were first done using the full set of sixty combinations of waves and isobars. At each energy the following procedure was carried out. First, 10,000 vectors A were generated at random. The likelihood for each was calculated with a subset of 600 events. The twelve sets A having the greatest likelihood were kept for use as starting vectors for the likelihood-maximizing procedure. The twelve initial vectors converged to typically four solutions (local maxima in likelihood.) These local maxima clustered into typically two groups; within a group the maxima were very near each other, but between groups

they were quite distinct. The statistical significance of the difference in the values of  $\mathcal{F}$  for two solutions,  $\mathcal{F}_1$  and  $\mathcal{F}_2$ , may be estimated by comparing this difference with the standard deviation of the difference  $\mathcal{F}_1 - \mathcal{F}_2$ , as defined by

$$\delta(\mathcal{F}_1 - \mathcal{F}_2) \equiv \frac{1}{N} \sum_c \sum_{i=1}^{N^c} (\log p_1^c(w_i^c) - \log p_2^c(w_i^c) - X)^2$$

$$\text{where } X \equiv \frac{1}{N} \sum_c \sum_{i=1}^{N^c} (\log p_1^c(w_i^c) - \log p_2^c(w_i^c)). \quad (15)$$

This  $\delta(\mathcal{F}_1 - \mathcal{F}_2)$  is the standard deviation of the difference  $\mathcal{F}_1 - \mathcal{F}_2$  for different sets of events generated from the same distribution as ours, i.e. events from other experiments equivalent to ours. If  $\mathcal{F}_1 - \mathcal{F}_2 \gg \delta(\mathcal{F}_1 - \mathcal{F}_2)$  then solution one may be assumed to have a statistically higher likelihood. (For this reasoning to be strictly true, the uncertainty in the amount that  $\mathcal{F}$  changes when the solution is refitted to a different set of events must be much smaller than  $\delta(\mathcal{F}_1 - \mathcal{F}_2)$ . Since  $N\mathcal{F}$  is a generalized chi square, it changes by the amount  $n_k \pm \sqrt{n_k}$ . Thus  $\delta(\mathcal{F}_1 - \mathcal{F}_2)$  must be much greater than  $\frac{\sqrt{n_k}}{N}$ . This is true in our case where  $\frac{\sqrt{n_k}}{N} = 0.001$  and  $\delta(\mathcal{F}_1 - \mathcal{F}_2) \approx 0.01$ .) The likelihoods for our solutions were usually all statistically equivalent by this  $\delta(\mathcal{F}_1 - \mathcal{F}_2)$  test.

The next step was to remove waves from each solution that were not statistically significant. The waves in each solution having magnitudes no larger than their errors (calculated from the error matrix) were removed first. The maximizations were done again with the reduced set of waves. The process was repeated until no waves were statistically unimportant. This method of eliminating unimportant

waves runs into trouble if there are large correlations among the waves. To guard against this, the reduction of a set of waves was only considered valid if the function  $N\mathcal{L} \equiv \log \mathcal{L}$  did not drop by much more than one for each wave removed. Judging from our error matrix, our largest correlations are roughly thirty percent and most waves have less than fifteen percent correlation with all other waves.

The effect on the wave-removing procedure of correlations among the waves may be visualized with the aid of error ellipses. The dependence of the likelihood on the magnitude of the  $i$ -th complex component of  $A$ ,  $|A_i|$ , and the magnitude of the  $j$ -th complex component,  $|A_j|$ , is indicated by the two-dimensional error ellipses in Fig. 3b. The centers of the ellipses correspond to a local maximum.

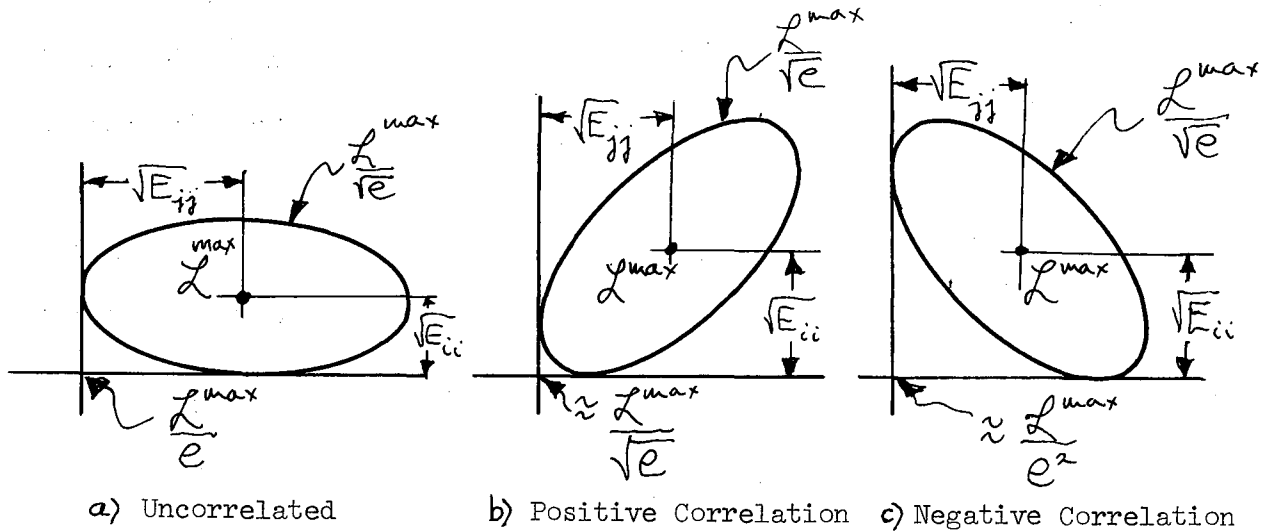


Fig. 3b. The Effect of Correlations on the Drop of Likelihood

The two waves in a) are uncorrelated.  $|A_i|$  and  $|A_j|$  each differ from zero by their errors,  $\sqrt{E_{ii}}$  and  $\sqrt{E_{jj}}$ . When  $A_i$  is set to zero,  $\mathcal{L}$  drops by  $\frac{1}{e}$  and when  $A_j$  is then removed,  $\mathcal{L}$  again drops by  $\frac{1}{e}$  to  $\frac{\mathcal{L}^{max}}{e^2}$ .

The waves in b) are positively correlated. Although each is one standard deviation from zero as in a),  $\mathcal{L}$  only drops by just over  $\frac{1}{\sqrt{e}}$  when they are both removed.

In c) the waves are negatively correlated. Here the likelihood  $\mathcal{L}$  drops by  $\frac{1}{e^2}$ , more than would be expected from looking only at  $\sqrt{E_{ii}}$  and  $\sqrt{E_{jj}}$ .

These considerations indicate that in general there may be several different subsets of the sixty-wave set that satisfy the criterion that  $\log \mathcal{L}^{\text{subset}}$  is not lower than  $\log \mathcal{L}^{60}$  by more than the number of waves removed. The intersection of these subsets will not necessarily satisfy the same criterion.

At each energy, our reduction process usually resulted in several sets of waves, each set containing about twenty-five waves.

Chains of solutions that were reasonably continuous from one energy to the next were then looked for. The longest chains found spanned three energies. As an attempt to produce a longer chain, a subset of 24 waves was put together that included waves which appeared to be important to solutions in most of the six energy bins. <sup>9</sup>

All solutions at each of the six energies were restricted to (or expanded to) this 24-wave set and the likelihoods re-maximized. Just one chain was found that connected more than two energies. This one chain connects all six energies and does so in a remarkably continuous manner. The remainder of this paper presents this solution, called the 24-wave solution.

### C. Kinematic Distributions

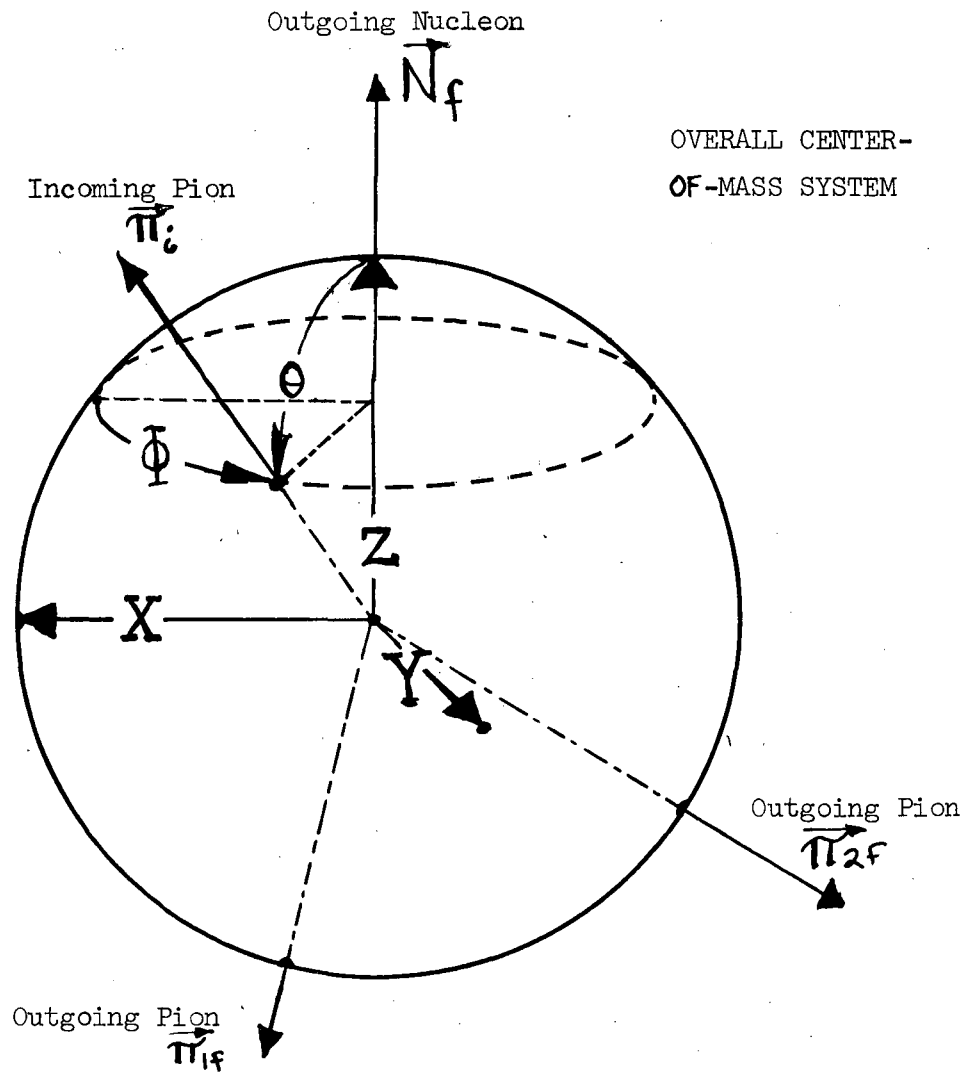
Four variables in addition to energy are required to specify completely the kinematics of an event. We use two diparticle masses and two angles. The diparticle masses are

$$\begin{array}{ll}
 M_{\pi\pi} & \text{Mass of the } \pi\pi \text{ diparticle} \\
 M_{N\pi} & \left\{ \begin{array}{l} \text{For } \pi^- \text{ incident: mass of } N\pi^- \text{ diparticle} \\ \text{For } \pi^+ \text{ incident: mass of } N\pi^+ \text{ diparticle.} \end{array} \right.
 \end{array}$$

The angles are  $\Theta$  and  $\Phi$ , the polar coordinates of the incoming pion in the special coordinate system given in Fig. 4. The X-Z plane contains the three outgoing particle momenta; the outgoing nucleon momentum is in the Z-direction; the Y-axis is in the direction of  $\vec{N}_f \times \vec{\pi}_{1f}$  where  $\vec{N}_f$  is the final nucleon momentum and  $\vec{\pi}_{1f}$  is the momentum of the pion with the same charge as the incident pion. The phase-space distribution of  $\cos \Theta$  is flat from -1 to 1 and the phase-space distribution of  $\Phi$  is flat from 0 to  $2\pi$ . The phase-space distributions of  $M_{\pi\pi}^2$  and  $M_{N\pi}^2$  are flat within the physically allowed region. Parity conservation introduces a restriction, namely the distribution of events is symmetric about  $\Phi = \pi$ .

In this section, kinematic distributions are presented for the data and the  $2^4$ -wave solution in the 1730 MeV energy bin. This bin is typical; the results in the other five energy bins are similar.

Figs 9a, 9b, and 9c plot the events in the 1730 MeV energy bin in each of the three charge channels (given for example in Fig. 1). Inside the large square are Dalitz scatter plots. The events in each Dalitz plot come from a different bin in  $\Phi$  and  $\cos \Theta$ . The bin in  $\Phi$  and  $\cos \Theta$  is indicated by the position of the small Dalitz plot in the large square. The large square is marked in  $\Phi$  and  $\cos \Theta$ ; it



$\vec{\pi}_{1f}$  has the same charge as the incoming pion,  $\vec{\pi}_i$ .

$\vec{\pi}_{1f}$ ,  $\vec{\pi}_{2f}$ , and  $\vec{N}_f$ , the final particle momenta, all lie in the X-Z plane.

$\vec{N}_f$  is along the Z-axis.

The Y-axis is in the direction of  $\vec{N}_f \times \vec{\pi}_{1f}$ .

Fig. 4. Definition of the Kinematic Variables and the Coordinate System

is divided into 16 bins and the lower left corner of each bin coincides with the lower left corner of its Dalitz plot. The Dalitz plots on the top row contain the events of all four Dalitz plots directly below and those in the right column contain the events of all plots to the left. The Dalitz plot at the top right contains all the events.

The kinematic distributions predicted by the 24-wave solution are compared with the data in Figs. 10a, 10b, and 10c. The scatter plots of the previous figures are binned into  $4 \times 4 =$  sixteen bins. The dashed tombstones indicate the data in each bin. The population is proportional to the height (or width) of the tombstone. (The dashed histograms on the top and right side of each small plot are again projections of what is immediately below and to the left.) The solid tombstones and histograms represent the distribution predicted by the model.

Figs. 11a, 11b, and 11c present the same data and solution but with the order of binning reversed.

Figs. 10 and 11 permit us to check graphically that the 24-wave solution predicts the distribution of events well in all areas of the four-dimensional kinematic space in all three channels. For a quantitative check, Table 1 presents chi-squares corresponding to the four-dimensional histograms. Chi-squares are calculated for different combinations of the four kinematic variables. All fifteen possible combinations are taken; each chi-square is labeled by a list of the variables simultaneously binned. The column labeled '#bins' indicates the number of non-empty bins. The last line of Table 1 presents chi-squares for the case where each of the four variables is divided into four bins. The number of bins for these chi-squares is slightly less than the possible 256 because of empty bins. The sum of the three chi-squares on this last



line is called the 'total chi-square',  $\chi^2_{\tau}$

The chi-squares approach their expected values when the number of bins increases. The model is best at following the large variations in the event distribution over the four-dimensional space; it lacks the higher degree of precision necessary to obtain good chi-squares in the cases of few bins with many events in each bin.

Table 2 lists the values of the total chi-square  $\chi^2_{\tau}$  for all six energy bins. The  $\chi^2_{\tau}$  for the highest energy bin is significantly greater than the others. This probably reflects the fact that more partial waves contribute to the reaction as the energy increases. The values of  $\mathcal{F}$  are also listed. These agree with the value of  $\mathcal{F}$  found for the artificial experiment described earlier (in section IIIC). This indicates that our 24-wave solution is a reasonable result of the maximum-likelihood analysis and that we are using roughly the proper number of waves for the quantity of data that we have.

#### D. Partial-Wave Cross Sections

An incoming partial wave is defined by the quantum numbers L, I, and J. Twelve incoming partial waves are included in the twenty-four waves of our solution. The model predicts a cross section for each of these partial waves. The cross section for the partial wave (L,I,J) in channel c is

$$\Sigma_{LIJ}^c \equiv \int_{\text{phase-space}} dw^4 \sum_{\mu=1}^4 \left| \sum_{k \in S_{LIJ}} A_k X_{k\mu}^c(w) \right|^2 \quad (16)$$

where the sum over k includes just those waves with incoming quantum numbers L, I, and J.

We define  $\sum_{LIJ}$  to be the sum of  $\sum_{LIJ}^c$  over all five possible  $N\pi \rightarrow N\pi\pi$  charge channels,

$$\begin{aligned}
 p\pi^- &\rightarrow n\pi^0\pi^0 & c=1 \\
 p\pi^- &\rightarrow n\pi^+\pi^- & c=2 \\
 p\pi^- &\rightarrow p\pi^-\pi^0 & c=3 \\
 p\pi^+ &\rightarrow p\pi^+\pi^0 & c=4 \\
 p\pi^+ &\rightarrow n\pi^+\pi^+ & c=5.
 \end{aligned} \tag{16a}$$

This sum is somewhat unconventional since two initial states are summed over (it will be seen later that this sum simplifies the mathematics by permitting cross terms to cancel).

$$\sum_{LIJ} \equiv \sum_{c=1}^5 \sum_{LIJ}^c.$$

$\sum_I$  is defined as the sum over L and J of  $\sum_{LIJ}$ :

$$\sum_I \equiv \sum_{LJ} \sum_{LIJ}.$$

Relations among the vector-addition coefficients for isospin are such that  $\sum_I$  may equivalently be written

$$\sum_I = \sum_{c=1}^5 \int_{\text{phase-space}} d^4w \sum_{\mu=1}^4 \left| \sum_{k \in S_I} A_k X_{k\mu}^c(w) \right|^2 \tag{17}$$

where the sum over k includes those waves with isospin I. The cross terms in this equation between waves with different L or J add to zero when summed over c (compare with Eq. 16).

Finally,  $\sum^{\text{TOTAL}}$  is defined as  $\sum^{\text{TOTAL}} \equiv \sum_{I=\frac{1}{2}} + \sum_{I=\frac{3}{2}}$ .

The same vector-addition relations imply that

$$\sum^{\text{TOTAL}} = \sum_{c=1}^5 R^c. \tag{18}$$

The overall scale for our model is adjusted so that  $\sum^{\text{TOTAL}}$  equals

our experimentally known value for the sum of the inelastic cross sections over the five charge channels.

Fig. 12 gives our experimentally known  $\Sigma^{\text{TOTAL}}$  over a large energy range including the range of this experiment. The experimentally known values of  $\Sigma_I$  are also given for completeness. The effect of the  $D_{15}$  and  $F_{15}$   $\pi N$  resonances in our energy region is clear.

Estimates of the  $\Sigma_{\text{LIJ}}$  may be obtained from elastic experiments by assuming that each partial wave of  $\pi N$  feeds either  $\pi N$  or  $\pi\pi N$ . The  $\Sigma_{\text{LIJ}}$  is then  $\pi k^2 (J+\frac{1}{2})(1-\eta^2)$  where  $\eta$  is obtained from elastic partial-wave analysis. The above assumption is reasonable since the cross section for the states  $p\pi^-$  and  $p\pi^+$  to proceed to other than  $N\pi$  and  $N\pi\pi$  is less than two millibarns (out of  $\sim 30$  millibarns). Fig. 13 compares the  $\Sigma_{\text{LIJ}}$  partial-wave cross sections predicted by our model with those predicted by elastic partial-wave analysis. It should be remembered that these cross sections are the sums of those for both the  $p\pi^-$  and  $p\pi^+$  initial states.

The elastic partial-wave analysis results in Fig. 13 are an average of the results of several groups<sup>7</sup>. The thick error bars in the figure indicate the root-mean-square fluctuations of the individual partial-wave analyses.

The dots in Fig. 13 are the values predicted by our model. The thin error bars are errors estimated from the error matrix.

In most cases our results agree qualitatively with the elastic partial-wave analyses. The greatest disagreement is for the  $F_{35}$  wave. Here, there is also the largest disagreement among the results of the different partial-wave analyses.

E. T - Matrix Elements

In Eq. 2 we introduced T-matrix elements  $T_k$  but immediately factored out the kinematic part  $X_{k\mu}^c$  (see Eq. 4). We did our fitting and continuity checking with the  $A_k$  because these are expected to vary more slowly with energy (since they do not contain such things as the production centrifugal-barrier factor). The T-matrix elements are useful for display purposes since they are more simply related to the cross section.

The T-matrix elements  $t_k$  are complex numbers having the same phases as the corresponding  $A_k$ . The amplitudes, however, are re-scaled as follows. If the amplitude  $A_k$  contributes the amount  $S_k^c$  to the cross section in channel c, then

$$4\pi \lambda^{2(J+\frac{1}{2})} |t_k^c|^2 = S_k^c \quad (19)$$

With this definition of the  $t_k^c$ , the unitary circle corresponds to  $|t_k^c| = \frac{1}{2} G_I^c$ .

$J$  is the total spin and  $I$  is the isospin of the k-th wave.

$G_I^c$  is the absolute value of the vector-addition coefficient for isospin

$I$  in charge channel c :

$I =$	$G_I^c$	$c =$	1	2	3	4	5
1/2		$\sqrt{\frac{2}{3}}$	$\sqrt{\frac{2}{3}}$	$\sqrt{\frac{2}{3}}$	0	0	
3/2		$\sqrt{\frac{1}{3}}$	$\sqrt{\frac{1}{3}}$	$\sqrt{\frac{1}{3}}$	1	1	

(20)

c indexes the charge channels as in Eq. 16a.

The exact relation between  $A_k$  and  $t_k^c$  is

$$t_k^c = A_k \cdot \sqrt{\frac{\sigma^{\text{TOTAL}} \sum_{\mu=1}^4 \int_{\text{phase-space}} |X_{k\mu}^c(w)|^2 d^4w}{\Sigma^{\text{TOTAL}} 4\pi \lambda^{2(J+\frac{1}{2})}}} \quad (21)$$

where  $\sigma^{\text{TOTAL}} \equiv \sum_{c=1}^5 \sigma^c$  is the sum of the experimentally

known cross sections (given for example in Fig. 12).

To avoid the necessity of listing the  $t_k^c$  separately for each of the incoming and outgoing channels, a 'total' T-matrix element  $t_k$  (without the superscript  $c$ ) is defined having the same phase as each  $t_k^c$  and having magnitude such that

$$|t_k|^2 = \sum_{c=2,3,4} |t_k^c|^2 . \quad (21)$$

Here the sum extends over the three channels  $c$  in which we have events:

$$\begin{array}{l} p\pi^- \rightarrow n\pi^+ \pi^- \\ p\pi^- \rightarrow p\pi^0 \pi^- \\ p\pi^+ \rightarrow p\pi^+ \pi^0 . \end{array} \quad (22)$$

Combining Eqs. 20 and 21, the unitary circle for  $t_k$  is

$$|t_k| = \begin{cases} \frac{1}{2}\sqrt{\frac{4}{3}} = 0.58 & \text{if wave } k \text{ has isospin } \frac{1}{2} \\ \frac{1}{2}\sqrt{\frac{5}{3}} = 0.65 & \text{if wave } k \text{ has isospin } \frac{3}{2} . \end{cases} \quad (23)$$

The reader is cautioned that this definition differs slightly from the usual definition that the unitary circle is at  $\frac{1}{2}$ .

Figs. 14a through 14f present the  $t_k$  for the 24-wave solution at each of the six energies. The overall phase at each energy is not determined by the fits. Anticipating continuity, we adjust the overall phase of the solution at each energy in the following way before plotting in Figs. 14 (and 15). The phase at each successive energy  $j$  was adjusted to minimize the sum

$$\sum_k \left| t_k(j) - t_k(j-1) \right|^2 , \quad j=2, \dots, 6.$$

However, two incoming waves,  $D_{15}$  and  $F_{15}$ , are known from elastic partial-wave analysis to resonate within our energy region. The waves having these incoming quantum numbers were therefore excluded from the sum over  $k$ .

After this adjustment is done, there is still one arbitrary overall phase; this phase is fixed for the purposes of display by changing the phase of all solutions at once so that wave one of the solution in the 1650 MeV bin is real (see Fig. 14a, wave  $\Delta$ PP11).

As discussed on pages 17 and 18, the error bars of Fig. 14 indicate the major and minor axes of the two-standard-deviation error ellipse. A larger uncertainty in phase than in amplitude appears generally to be the case.

In Fig. 15 each  $t_k$  is plotted individually against energy. Those waves  $k$  contributing to the incoming  $F_{15}$  and  $D_{15}$  partial waves are specially indicated.

The most striking feature of this solution is its continuity. Virtually all of the waves appear to be stationary in phase over the entire 160 MeV range of the analysis. This is surprising because one would expect that waves  $k$  fed by the  $F_{15}$  and  $D_{15}$  partial waves should move in a counter-clockwise direction with increase in energy. As indicated on Fig. 15, there are three waves  $k$  fed by  $F_{15}$  and two fed by  $D_{15}$ . The  $F_{15}$   $N\pi$  resonance is centered at 1690 MeV in the elastic channel with width  $\Gamma = 125$  MeV. The  $D_{15}$   $N\pi$  resonance is at 1675 MeV in the elastic channel with width  $\Gamma = 145$ . The contributions of these resonances to our inelastic channels is appreciable as may be seen in Fig. 13.

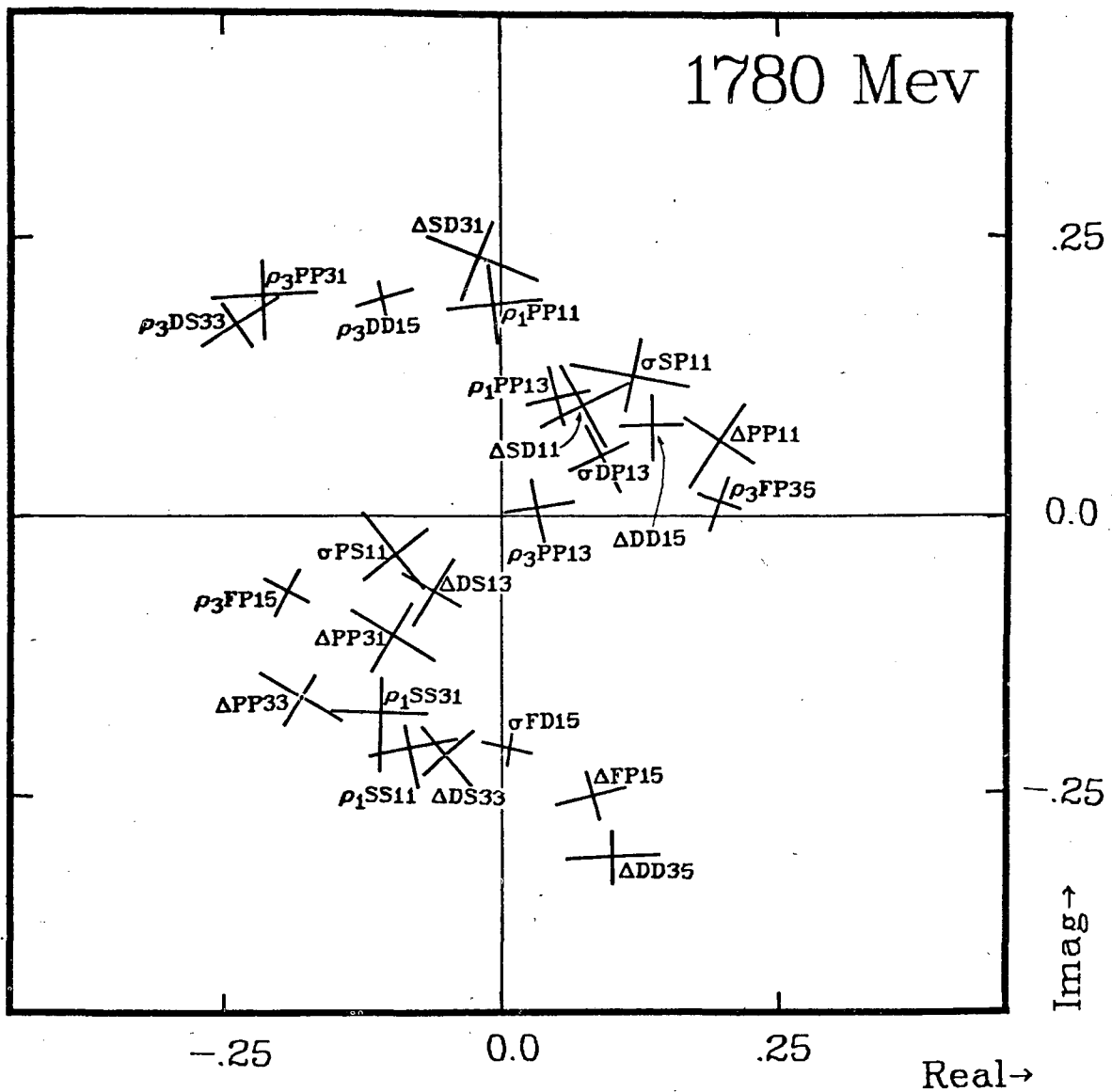
## V. CONCLUSION

We have looked at considerable length for maximum-likelihood solutions to our Iso-bar Model that are continuous over our 1640 to 1800 MeV energy region. Despite the generality of the model, only one candidate has appeared, the 24-wave solution. This solution is stable in that waves may be added to it or removed from it a few at a time without greatly altering the position of the likelihood maximum. Our 24-wave solution matches the kinematic distribution of events well and makes reasonable predictions for the partial-wave cross sections. But our solution is more continuous than would be desired. Where rapid phase changes are expected because of resonances in the elastic channel, there is almost no phase change at all (at least relative to the other waves fed by non-resonant partial waves).

If the  $F_{15}$  and  $D_{15}$  incoming partial waves were coupled to the  $N\pi\pi$  final state only through their resonances (described in the last section), then the phases of all five waves in our model fed by  $F_{15}$  and  $D_{15}$  should increase by about  $100^\circ$ , as the elastic  $N\pi$  phases do, from the low to the high end of our 160 MeV energy region. The apparent lack of this effect may be due in part to non-resonant components in the  $F_{15}$  and  $D_{15}$  intermediate-state formation amplitudes. From Fig. 13, a 30 or 40 percent non-resonant background appears to be present in  $D_{15}$  and in  $F_{15}$ . This could reduce the expected phase change to about  $60^\circ$ . It is also possible that the  $t_k$  for all waves slowly increase in phase with increasing energy by about  $20^\circ$  per 100 MeV. This would reduce the observed phase change in our  $F_{15}$  and  $D_{15}$  waves by another  $30^\circ$ .

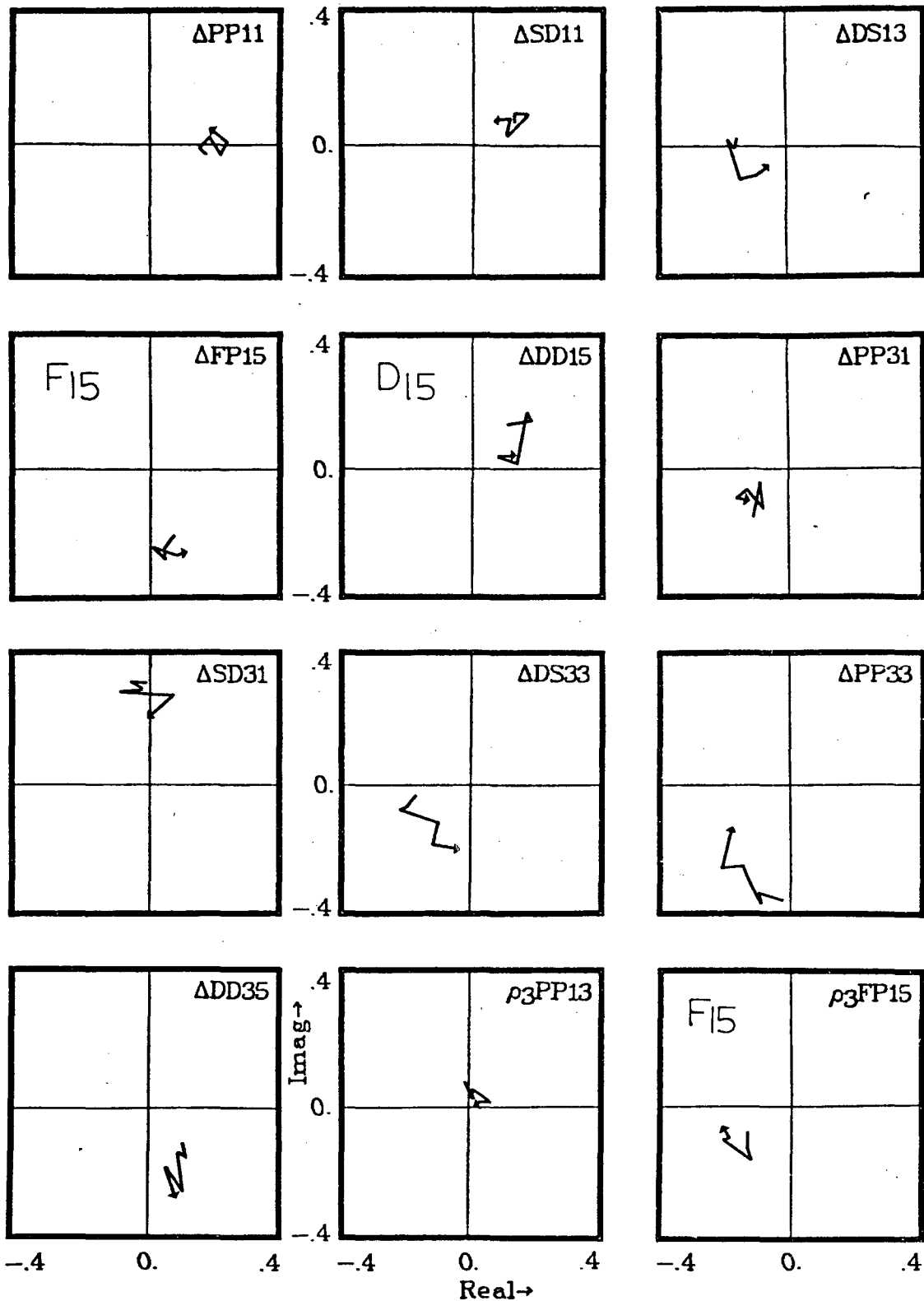
These explanations are too qualitative and incomplete to be satisfying. The results of our fits appear to be meaningful but we do not completely understand them. Work on this project is continuing and we expect eventually to cover the energy region 1500 to 2000 MeV. Ref. 11 gives the next proposed piece of literature from this experiment.





Error Bars are Major and Minor Axes of  $2\sigma$  Error Ellipse.

Fig 14f T-MATRIX ELEMENTS at 1780 MeV



Tail is 1650 Mev.  
Arrow is 1780 Mev.

Fig 15 ARGAND PLOTS OF  $t_k$  FOR EACH  $k$

APPENDIX

COMPUTER UTILIZATION

The complexity of the model and the large number of events necessitate the use of special computer methods. Computations are broken into series of procedures with the intermediate results stored on tape. This enables one to alter a portion of the formulae without re-doing the whole calculation. To achieve flexibility a group of two large and roughly eight smaller programs has been created. These programs pass data among each other and to later runs of themselves by writing and reading magnetic tape and by punching and reading cards. The tape formats and card formats are uniform within the group.

A flow chart indicating the programs in this group (called the Rumble Group) is given in Fig. 16. The program TRIA2<sup>12</sup> generates the complex numbers  $X_{ku}^C$  for each event. These are represented by  $2n_k$  real numbers which are packed two per 60-bit computer word and stored on tape. The packing consists simply of retaining the most significant 30 bits of the CDC 6600 floating-point representation of each number and placing these alternately in the upper and lower 30 bits of the 60 bit words to be written on tape. This packing reduces the number of tapes required and increases computing efficiency by reducing the number of memory fetches during subsequent computations involving the  $X_{ku}^C$ .

Normalization Integral

To obtain the normalization integral  $R^C$ , several intermediate steps are taken. The following relation makes it possible to obtain  $R^C$  by

ACKNOWLEDGEMENTS

I am grateful to Art Rosenfeld who has shown much interest, encouragement, and support, and to Dave Herndon and Ron Longacre, with whom I share this immense undertaking; we are in it together. I am grateful to Roger Cashmore, who has provided much stimulation, persuasion, and brute-force coercion to keep this project in order. Je veux rémercier Gerard Smadja pour ses bonnes idées théoriques. And finally, I am indebted to Orin Dahl, Jerry Friedman, Paul Hoch, Ron Huesman, Maxine Matison, Serban Protopopescu, Andris Skuja, and Vic Waluch, who kept me hanging on.

contracting a matrix  $W_{kk'}^c$ , (defined in Eq. 24 below) with the vector  $[A_k]$ .  $W_{kk'}^c$ , does not depend on the numbers  $A_k$  so it is calculated only once.

$$R^c = \int_{\text{phase-space}} \sum_{\mu=1}^4 \sum_{k=1}^{n_k} \sum_{k'=1}^{n_k} A_k X_{k\mu}^c(w) A_{k'}^* X_{k'\mu}^{c*}(w) d^4w =$$

$$= \sum_{k=1}^{n_k} \sum_{k'=1}^{n_k} A_k A_{k'}^* W_{kk'}^c$$

where

$$W_{kk'}^c \equiv \sum_{\mu=1}^4 \int_{\text{phase-space}} X_{k\mu}^c(w) X_{k'\mu}^{c*}(w) d^4w \quad (24)$$

The integral of Eq. 24 is done by the Monte-Carlo method of generating events at random in phase space. Parameters  $X_{k\mu}^I$  (as defined below Eq. 4 but before charge projections are made) are calculated for each Monte-Carlo event by the program TRIA2. Here the superscript I indicates that the variable depends directly on total isospin and is independent of any particular charge channel. The  $X_{k\mu}^c$  and  $W_{kk'}^c$  will be obtained later from  $X_{k\mu}^I$  and  $W_{kk'}^I$ . The matrix  $W_{kk'}^I$  is obtained by averaging the product  $X_{k\mu}^I X_{k'\mu}^{I*}$  over the Monte-Carlo events. This is done in the program KREBS.

### Charge Channel

The  $X_{k\mu}^c$  for a given  $\rho$  or  $\sigma$  wave,  $k$ , depend on the charge channel  $c$  only through multiplication by a real vector-addition coefficient corresponding to the decomposition of the incoming isotopic-spin state into the isotopic spins of the final resonance and third particle. This is also true for  $\Delta$  waves if the addition of the third and fourth

terms on the right of Eq. 3 is deferred. To reduce computation, therefore, the special charge-channel-independent set  $X_{k\mu}^I$  is generated for the Monte-Carlo events. The deferred sum is done and the vector-addition coefficients are re-inserted after  $W_{kk}^I$  is calculated to obtain  $W_{kk}^c$ , for each charge channel  $c$ . The program STRETCH calculates these  $W_{kk}^c$  from the  $W_{kk}^I$ . The program MERGE makes it possible to improve statistical accuracy by averaging matrices  $W_{kk}^c$ , obtained from separate sets of Monte-Carlo events.

#### Starting Values for the Fits

The program SEEK generates starting sets of  $A_k$  at random: the real and imaginary parts of each  $A_k$  are selected at random between (typically) -1 and 1. For each set of  $A_k$  a quick estimate is made of our function  $\mathcal{F}$  using 600 of the events in the energy bin. Use of this small subset sacrifices accuracy of  $\mathcal{F}$  for computational speed. The sets of  $A_k$  giving the highest value of  $\mathcal{F}$  are punched on cards. SEEK will also make one- and two-variable plots of  $\mathcal{F}$ , such as Fig. 8.

#### Stepping Procedure

The maximum-likelihood stepping procedure is done by the program RUMBLE. The majority of computer execution time is spent in this program. The user specifies the set of waves to be used before each RUMBLE run. This set must be a subset of the waves on the real-event tape and in the normalization matrices  $W_{kk}^c$ . (Our tapes and normalization matrices contain the sixty waves given in Fig. 2.) RUMBLE copies the  $X_{k\mu}^c$  for the user-specified waves  $k$  from the real-event tapes to a scratch file. The same packed format is retained.

For each step in the fit, RUMBLE reads through the scratch file event by event performing the running sums for  $\mathcal{F}$  (Eq. 7),  $\nabla\mathcal{F}$  (Eq. 8),

( and  $\nabla \nabla^T$  if it is a Newton-Raphson step). Almost all of the execution time of RUMBLE is spent doing these running sums. Four machine-language subroutines in RUMBLE do the necessary calculations. These subroutines are constructed to take maximum advantage of parallel unit operation on the CDC 6600 computer.

For each event,  $p^c(w_i^c)$  is calculated from Eq. 4. Non-normalized addition is done within the sum over  $k$ . Evaluation of this equation requires roughly  $12n_k$  memory fetches,  $16n_k$  additions, and  $16n_k$  multiplications. The execution time is  $12n_k$  microseconds.

The derivative vector of  $p^c(w_i^c)$  is calculated using Eq. 7. The portion within large parentheses is available from the calculation of  $p^c(w_i^c)$ . Updating the  $2n_k$  components of the running sum for requires  $12n_k$  memory fetches,  $16n_k$  additions (again unnormalized),  $16n_k$  multiplications, and  $2n_k$  memory stores. The execution time is  $18n_k$  microseconds.

During Newton-Raphson steps, the upper triangle of the matrix  $M$  is calculated. For each event, updating the running sum for this upper triangle requires roughly  $2n_k^2$  memory fetches,  $2n_k^2$  multiplications,  $2n_k^2$  (normalized) additions, and  $2n_k^2$  memory stores. The execution time for this is  $3n_k(n_k+20)$  microseconds.

### Histograms

The program HSCRAB makes histograms of event population as a function of single kinematic variables. The curve representing the prediction of the model is superimposed and chi-squares are calculated.

The program RAWMEAT makes four-dimensional and two-dimensional scatter plots and histograms. Figs 9, 10, and 11 were made with RAWMEAT.



REFERENCES AND FOOTNOTES

1. S. J. Lindenbaum and R. B. Sternheimer, Phys. Rev. 123, 333 (1961), Phys. Rev. 105, 1874(1957), Phys. Rev. 106, 1107(1957), Phys. Rev. 109, 1723(1958).
2. F. T. Solmitz, Analysis of Experiments in Particle Physics, Annual Review of Nuclear Science, 14, 375(1964).
3. W. C. Davidon, Variance Algorithm for Minimization, Computer Journal, 10, 406(1967).
4. P. Eberhard and W. O. Koellner, Optime System for Fitting Theoretical Expressions, UCRL-20159, October 1970.
5. John Todd, Survey of Numerical Analysis (McGraw-Hill, 1962), p. 232.
6. J. Anderson, F. S. Crawford, Jr., and J. C. Doyle, Phys. Rev. 152, 1139(1967).
7. A. D. Brody, R. J. Cashmore, A. Kernan, D. W. Leith, B. G. Levi, B. C. Shen, J. P. Berge, D. J. Herndon, R. Longacre, L. R. Price, A. H. Rosenfeld, and P. Soding,  $\pi^-p$  Elastic Scattering in the C. M. Energy Range 1400 - 2000 MeV, Phys. Rev. D. 3, 2619(1971), also A. D. Brody, R. J. Cashmore, A. Kernan, D. W. Leith, B. G. Levi, A. Minten, B. C. Shen, J. P. Berge, B. Deler, D. J. Herndon, R. Longacre, L. R. Miller, A. H. Rosenfeld, P. Soding, Experimental Results on the Reactions  $\pi^-p \rightarrow \pi\pi N$  in the C. M. Energy Range 1400-2000 MeV, UCRL-20856, June 1971.
8. Bernard Deler, Contribution a la Diffusion Inelastique  $\pi^+p$  pour des Energies de  $\pi$  Incident Voisines de 1 GeV (Ph. D. Thesis), Centre d'Etudes Nucleaires de Saclay Report CEA-R-3579, May, 1969 (unpublished).
9. This twenty-four wave set was found by R. Longacre and D. Herndon.
10. D. J. Herndon, A. Barbaro-Galtieri, A. H. Rosenfeld,  $\pi N$  Partial-Wave Amplitudes, A Compilation, UCRL-20030  $\pi N$ , February 1970.

11. D. J. Herndon, A Partial-Wave Analysis of the Reaction  $\pi N \rightarrow \pi\pi N$  (Ph. D. Thesis, as yet unwritten), UC-LBL-544.
12. TRIA2 was written by D. J. Herndon. This program exists in two versions. The more general version will calculate the  $X_{k\mu}^C$  for any (two particles)  $\rightarrow$  (three particles) reaction using any resonances and any waves. Modifications of the output format are required if more than four combinations of helicities of the individual particles may occur. The more specialized version of TRIA2 achieves an increase in execution speed by being restricted to reactions in which the individual particles have the same spin and isotopic spin as those in our reaction,  $N\pi \rightarrow N\pi\pi$ . This program and the mathematical formulation of the  $X_{k\mu}^C$  will be described in a forthcoming paper (as yet unpublished): D. J. Herndon, A Generalized Isobar Model Formalism, UC-LBL-543.

Table 1. VARIOUS CHI-SQUARES FOR THE 24-WAVE SOLUTION AT 1730 MEV

<u>Variables Binned</u>	<u><math>\rho\pi^- \rightarrow \pi\pi^+ \pi^-</math></u>		<u><math>\rho\pi^- \rightarrow \rho\pi^- \pi^0</math></u>		<u><math>\rho\pi^+ \rightarrow \rho\pi^+ \pi^0</math></u>	
	<u><math>\chi^2</math></u>	<u># Bins</u>	<u><math>\chi^2</math></u>	<u># Bins</u>	<u><math>\chi^2</math></u>	<u># Bins</u>
$M_{N\pi}$	29.2	10	28.1	10	34.6	10
$M_{\pi\pi}$	21.8	12	23.6	12	31.6	12
$\cos \theta$	21.5	10	45.9	10	18.2	10
$\phi$	16.4	12	19.0	12	27.0	12
$M_{N\pi}$ $M_{\pi\pi}$	52.5	15	40.6	15	48.3	15
$M_{N\pi}$ $\cos \theta$	75.4	40	107.9	40	63.5	39
$M_{N\pi}$ $\phi$	56.8	48	53.8	48	87.4	48
$M_{\pi\pi}$ $\cos \theta$	72.8	40	79.3	40	61.8	40
$M_{\pi\pi}$ $\phi$	69.3	48	67.1	48	71.3	48
$\cos \theta$ $\phi$	7.5	16	36.4	16	27.9	16
$M_{\pi\pi}$ $\cos \theta$ $\phi$	195.1	192	225.4	189	180.1	185
$M_{N\pi}$ $\cos \theta$ $\phi$	144.1	151	200.4	157	137.6	144
$M_{N\pi}$ $M_{\pi\pi}$ $\phi$	206.8	179	184.8	178	188.5	171
$M_{N\pi}$ $M_{\pi\pi}$ $\cos \theta$	201.2	146	189.5	148	173.9	142
$M_{N\pi}$ $M_{\pi\pi}$ $\cos \theta$ $\phi$	236.8	228	260.2	229	210.8	213

Table 2. LOG-LIKELIHOODS AND 'TOTAL' CHI-SQUARES FOR EACH ENERGY BIN

<u>Energy Bin</u>	<u>Log <math>\mathcal{L}</math></u>	<u><math>\mathcal{F}</math> (<math>=1/N \text{ Log } \mathcal{L}</math>)</u>	<u><math>\chi^2</math></u>	<u># Bins</u>
1650	1492.7	.22982	699.1	633
1670	2654.0	.26752	817.4	684
1690	1588.7	.23852	733.0	666
1730	2590.2	.33771	685.3	666
1750	1305.1	.27281	663.0	649
1780	2773.4	.32129	1029.2	689

FIGURE CAPTIONS

	page
1. Quantum Numbers	3
2. The Sixty-Wave Set	6
3a. Two-Dimensional Projection of the Error Ellipse	17
3b. The Effect of Correlations on the Drop in Likelihood	24
4. Definition of the Kinematic Variables and the Coordinate System	27
5. Data Used in This Analysis	47
6. Typical Sixty-Wave Fit - Newton-Raphson Every Fifteenth Step	48
7. Comparison of Procedures for Typical Sixty-Wave Fit	49
8. $\sigma$ Versus Two of the A-Parameters With The Other A-Parameters at a Fitted Peak	50
9a, b, c. Four-Dimensional Scatter Plots at 1730 MeV	51
10a, b, c. Four-Dimensional Histograms at 1730 MeV	54
11a, b, c. Four-Dimensional Histograms With Axes Reversed	57
12. $N\pi$ Inelastic Cross Sections	60
13. Comparison of Partial-Wave Cross Sections	61
14a, b, c, d, e, f. T- Matrix Elements at Each Energy	62
15. Argand Plots of $t_k$ For Each k	68
16. The Rumble System	70



Fig. 5 Data Used In This Analysis

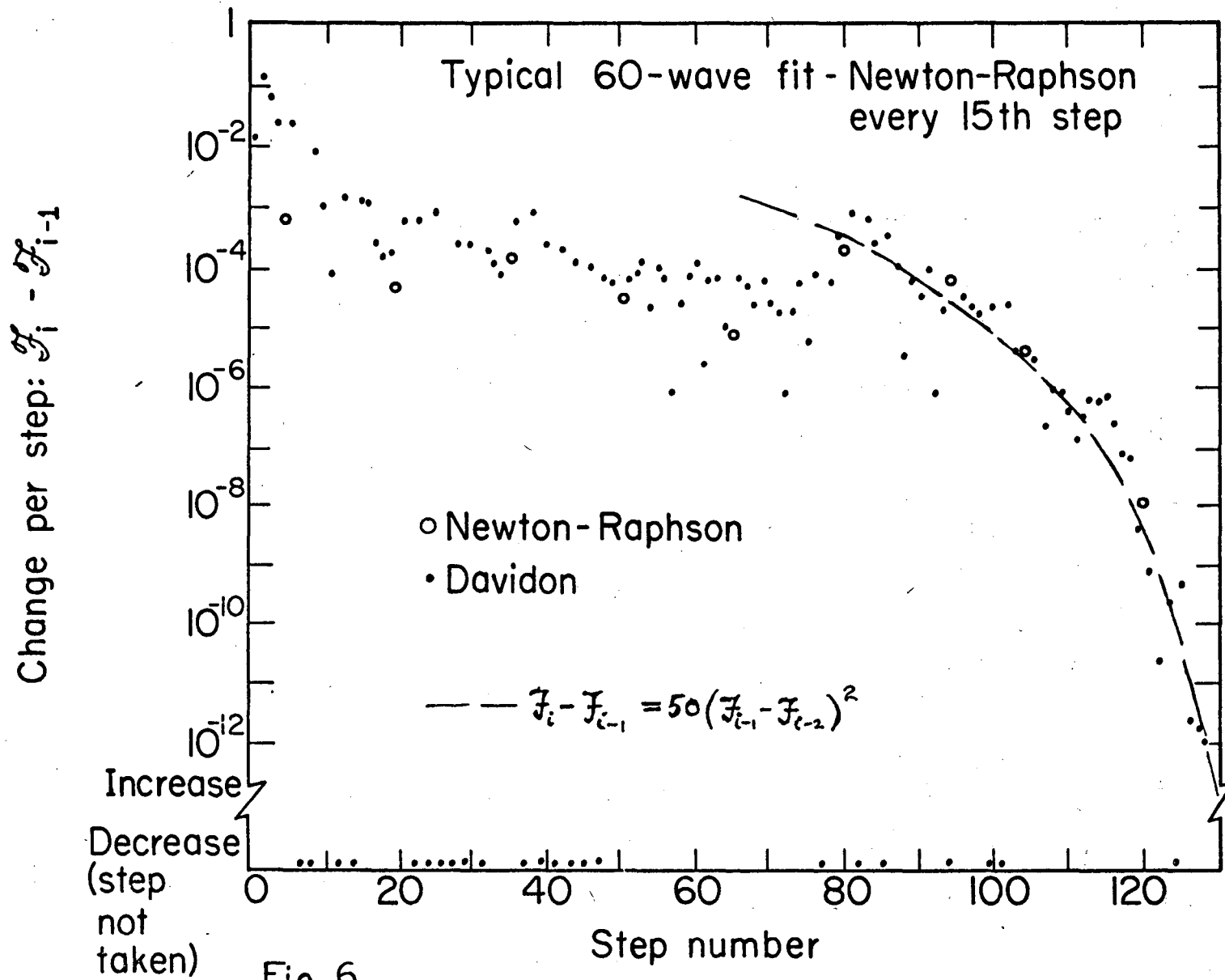
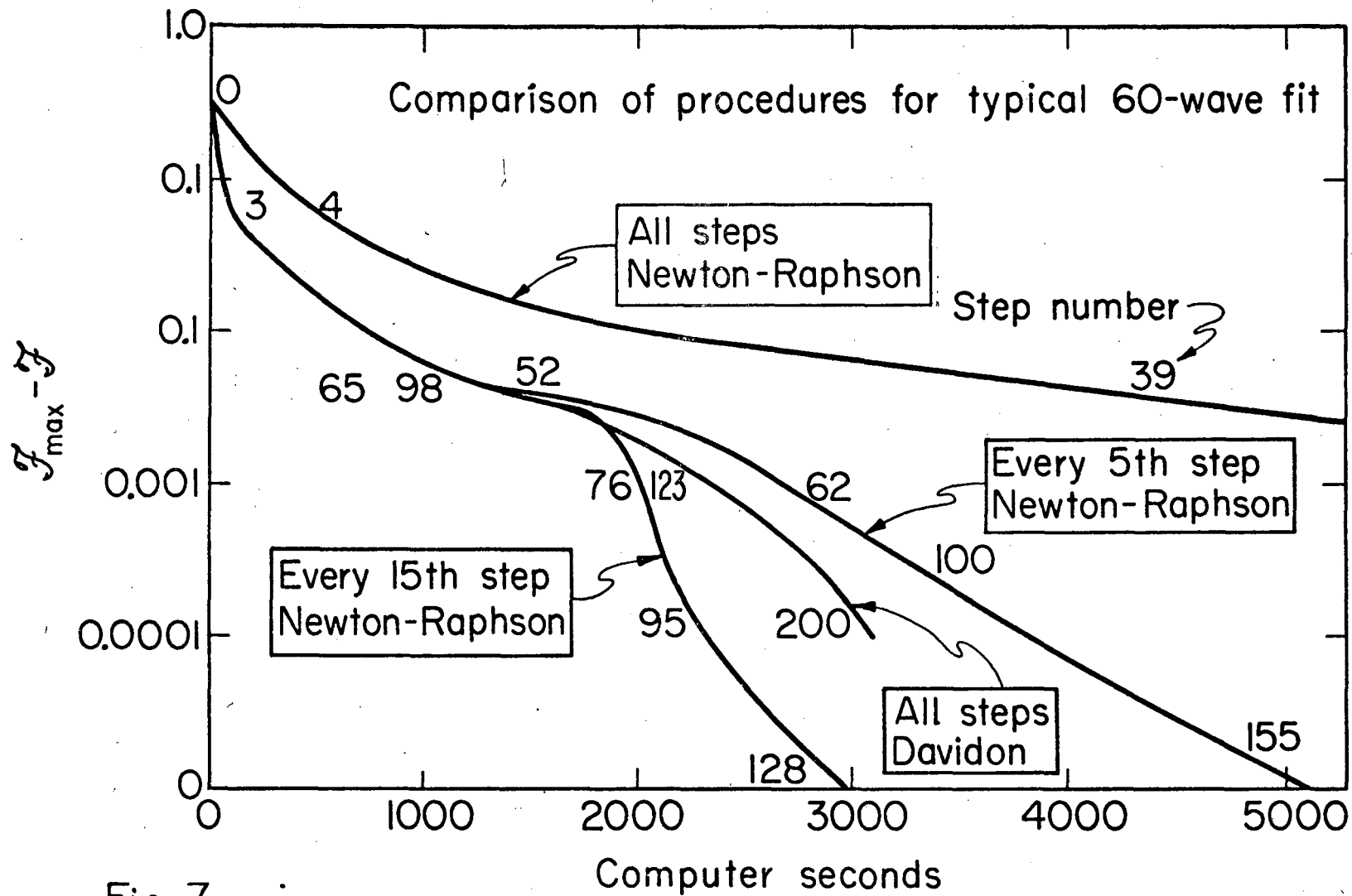


Fig 6

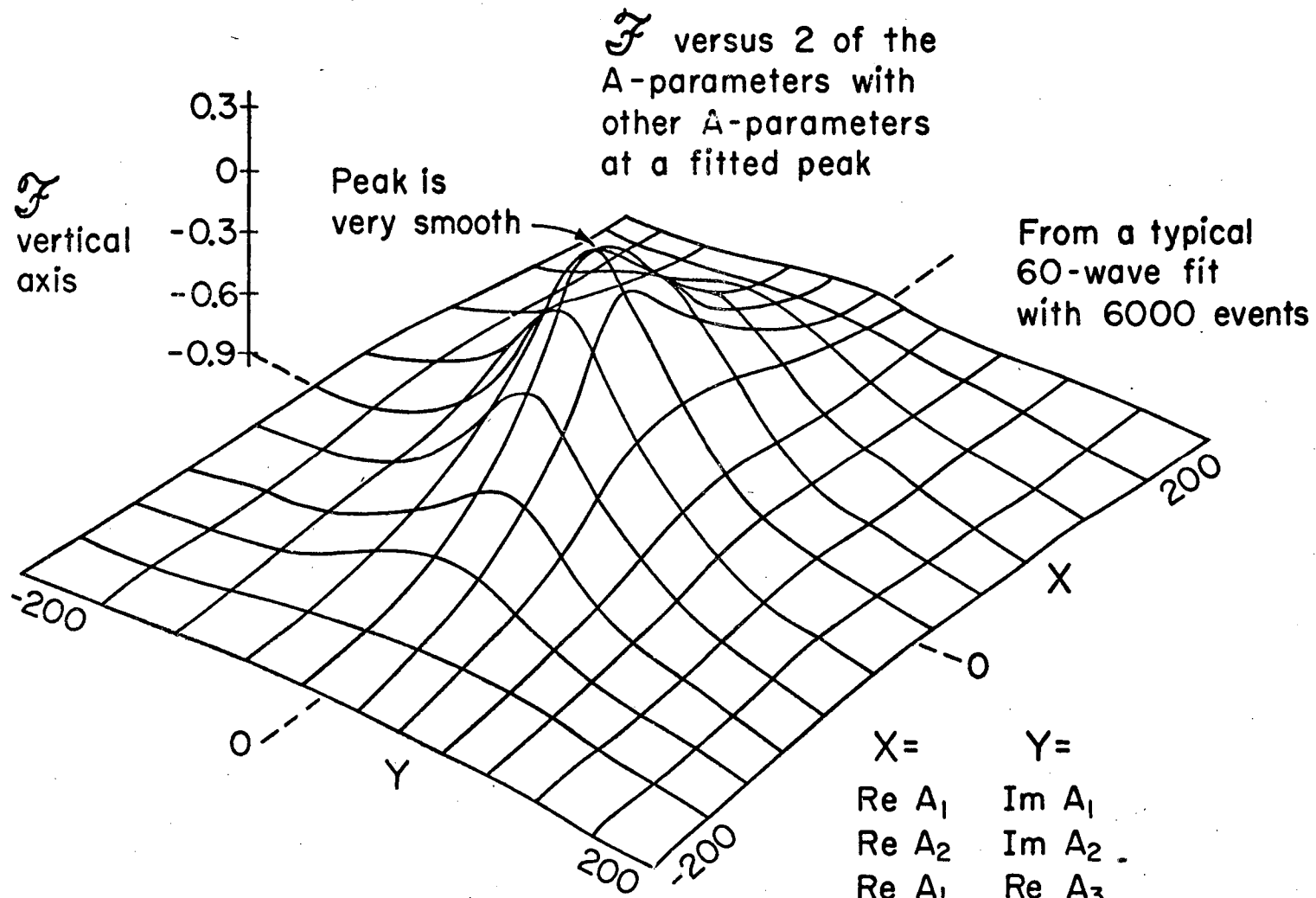
XBL 718-4180



-49-

Fig 7

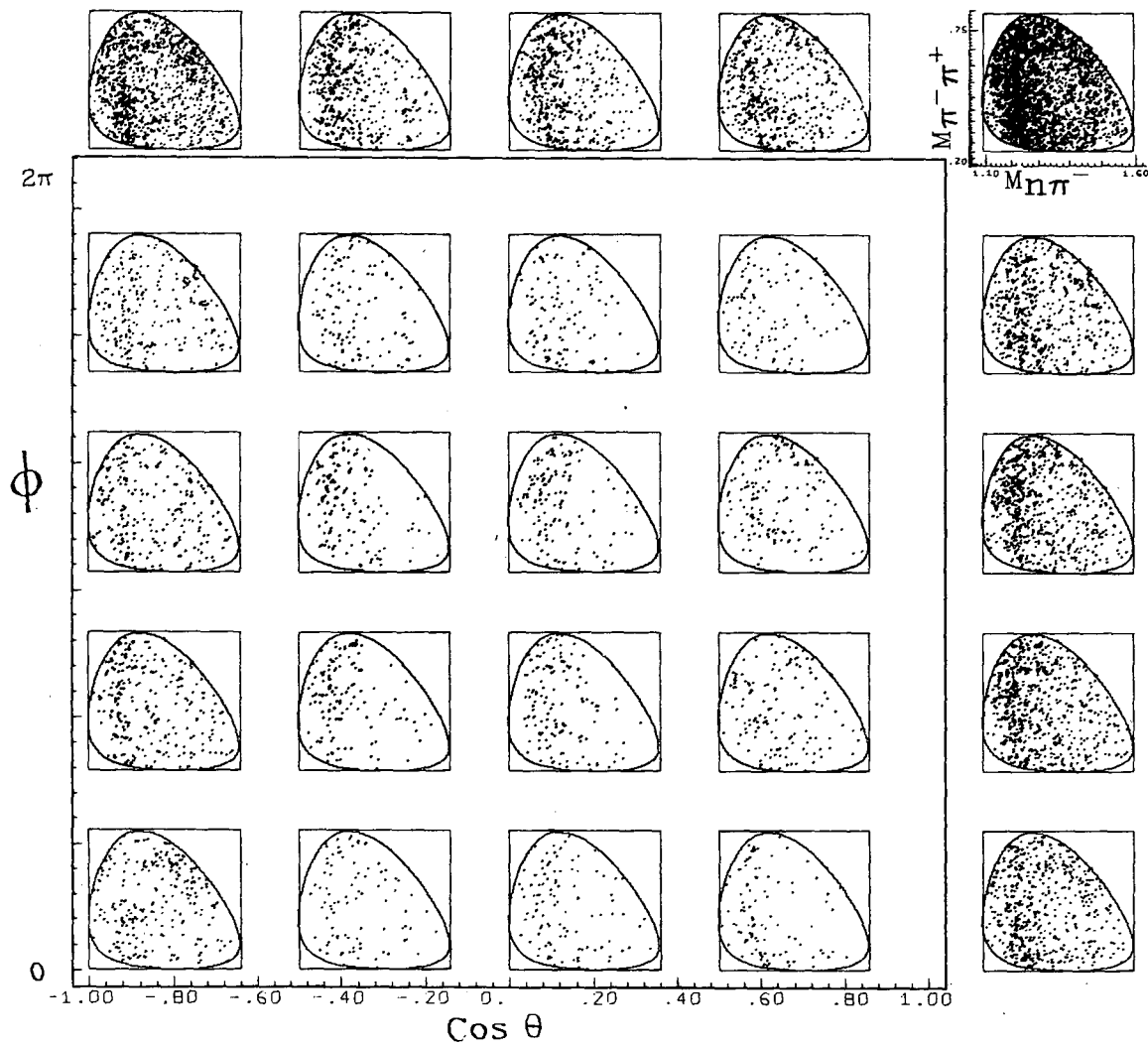
XBL718-4178



-50-

Fig 8



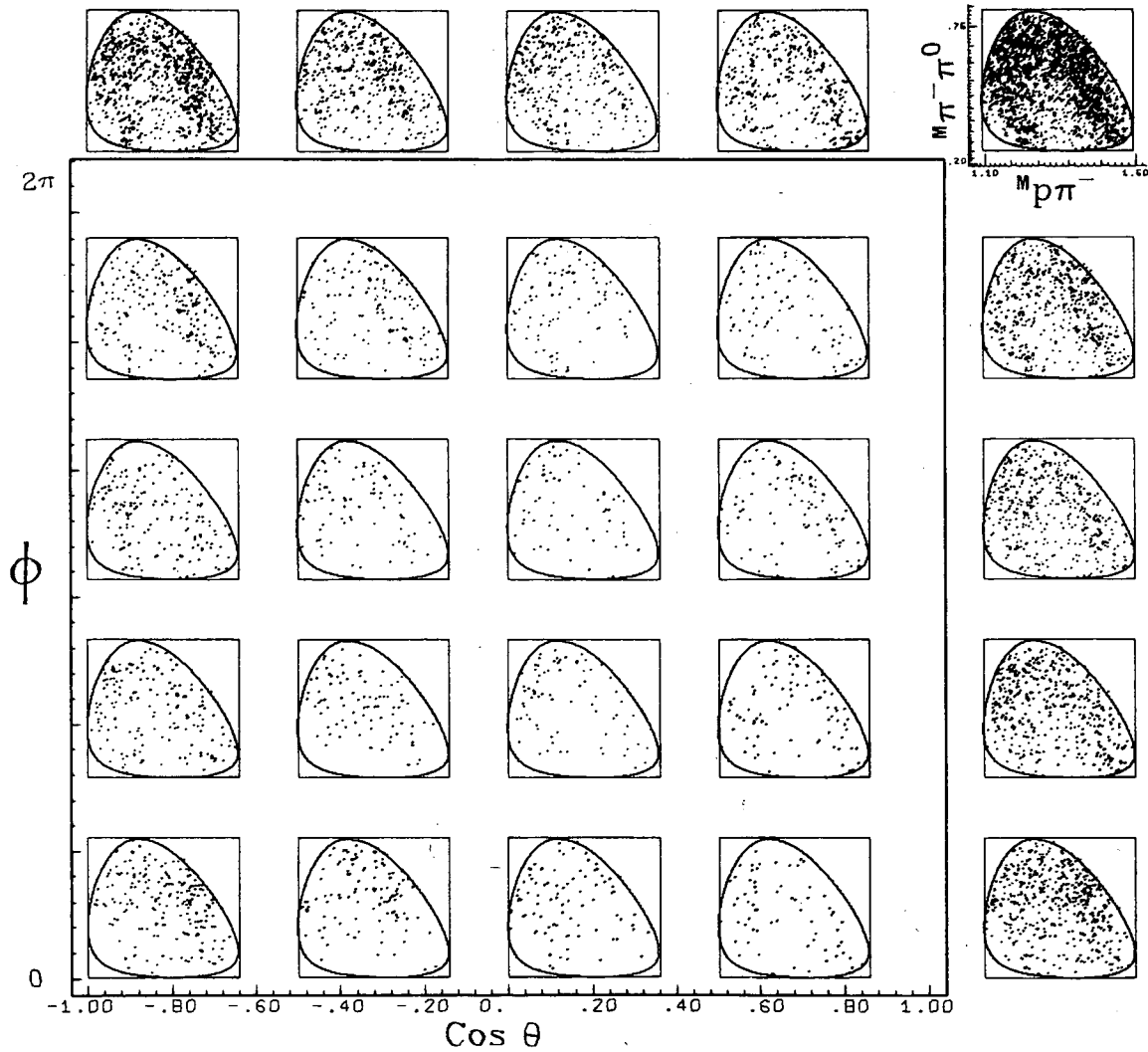


$p\pi^- \rightarrow n\pi^- \pi^+$

1730 Mev

Fig.9a. Four-Dimensional Scatter Plot

XBL 7112-1801

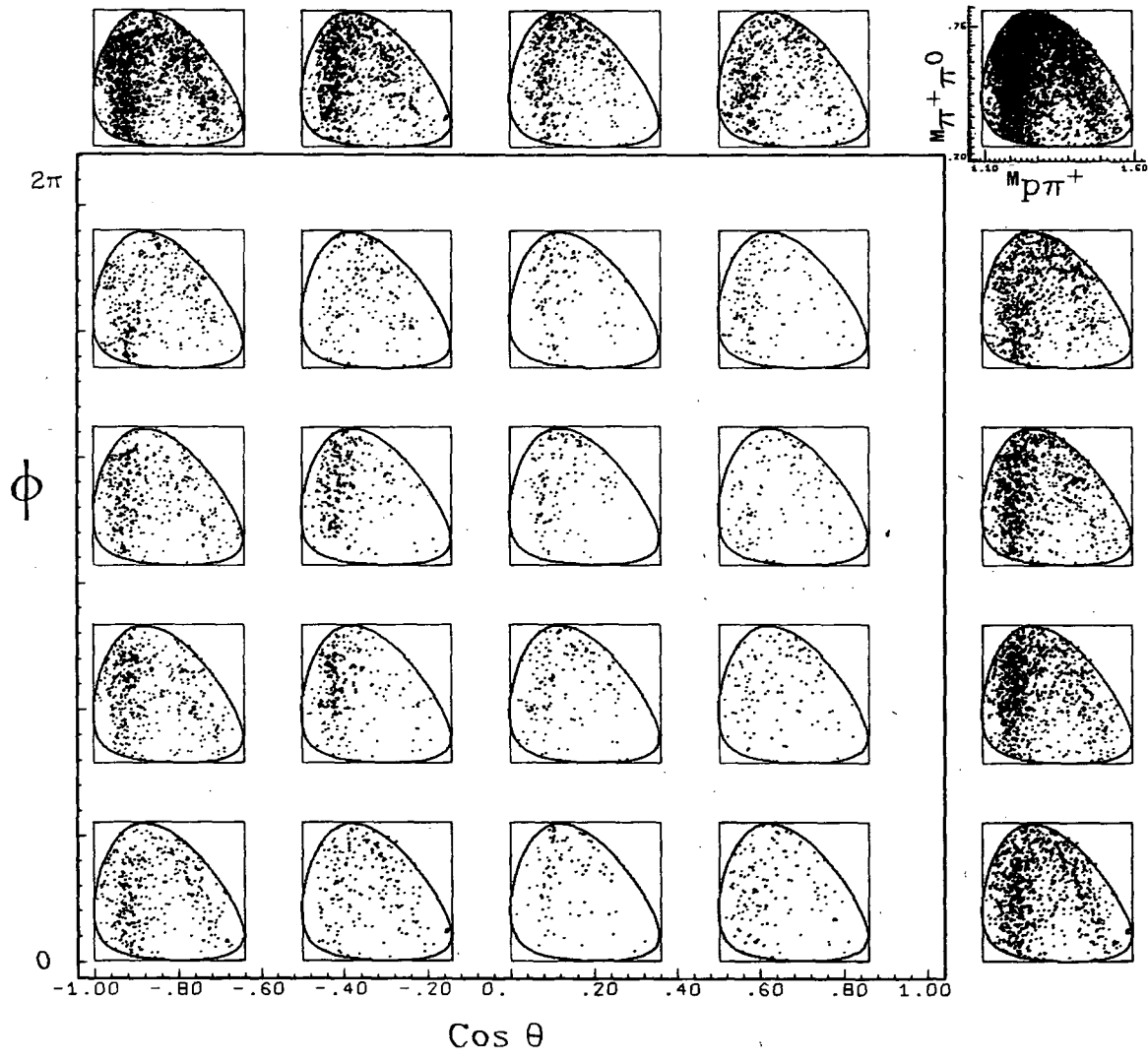


$p\pi^- \rightarrow p\pi^-\pi^0$

1730 Mev

Fig. 9b. Four-Dimensional Scatter Plot

XBL 7112-1802



$p\pi^+ \rightarrow p\pi^+\pi^0$

1730 Mev

Fig. 9c. Four-Dimensional Scatter Plot

XBL 7112-1800

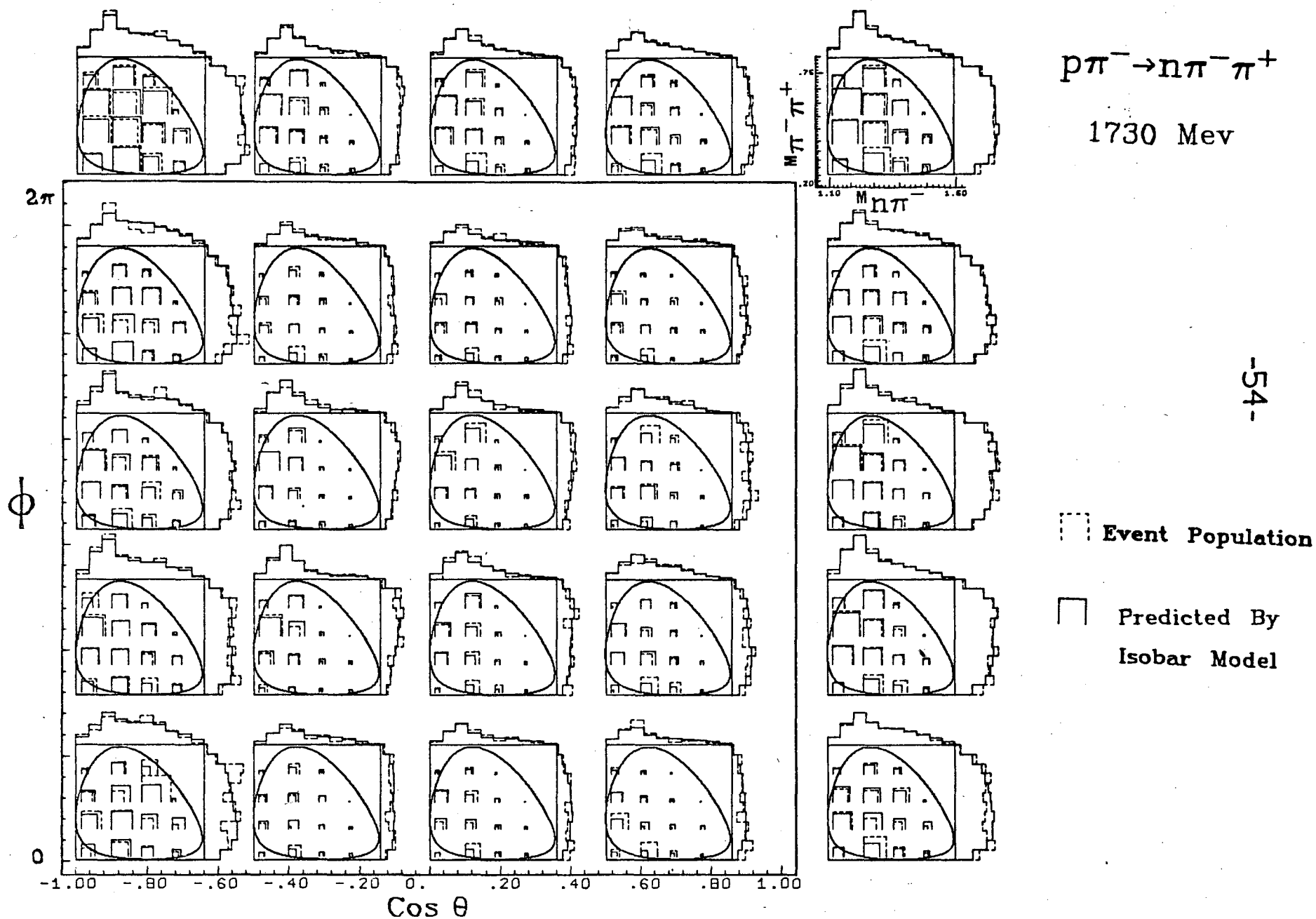


Fig. 10a

Four-Dimensional Histogram

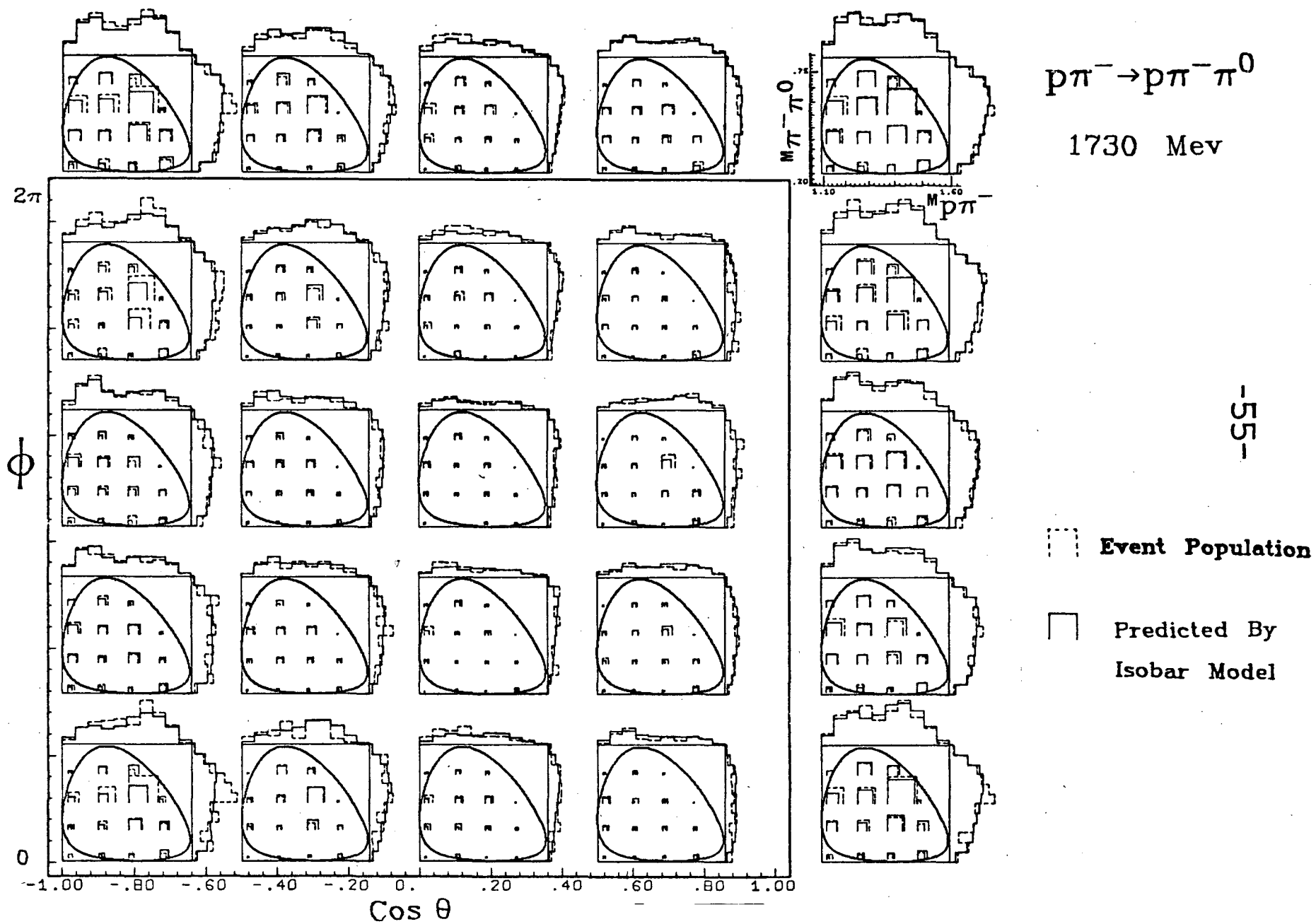


Fig. 10b Four-Dimensional Histogram

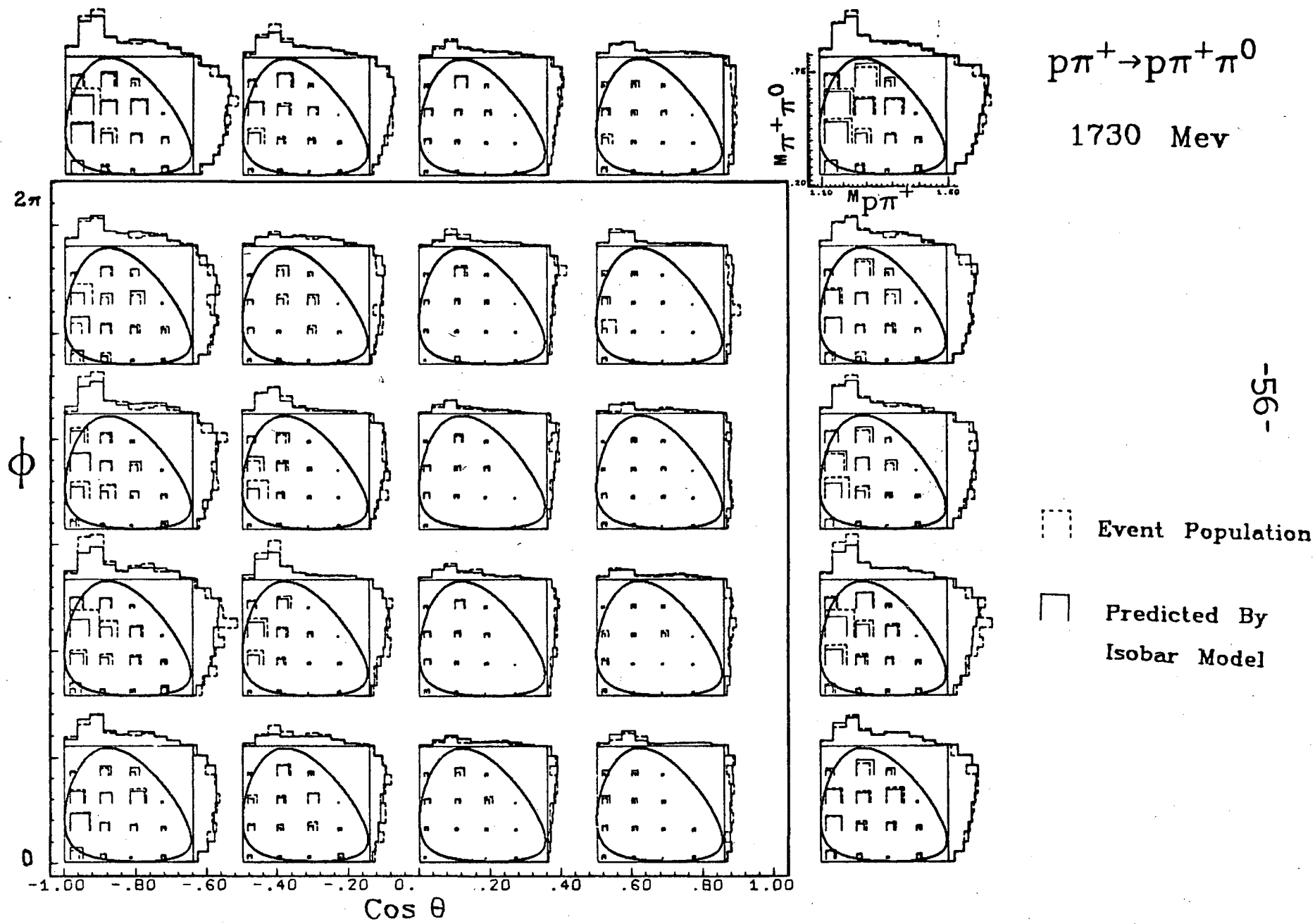


Fig. 10c Four-Dimensional Histogram

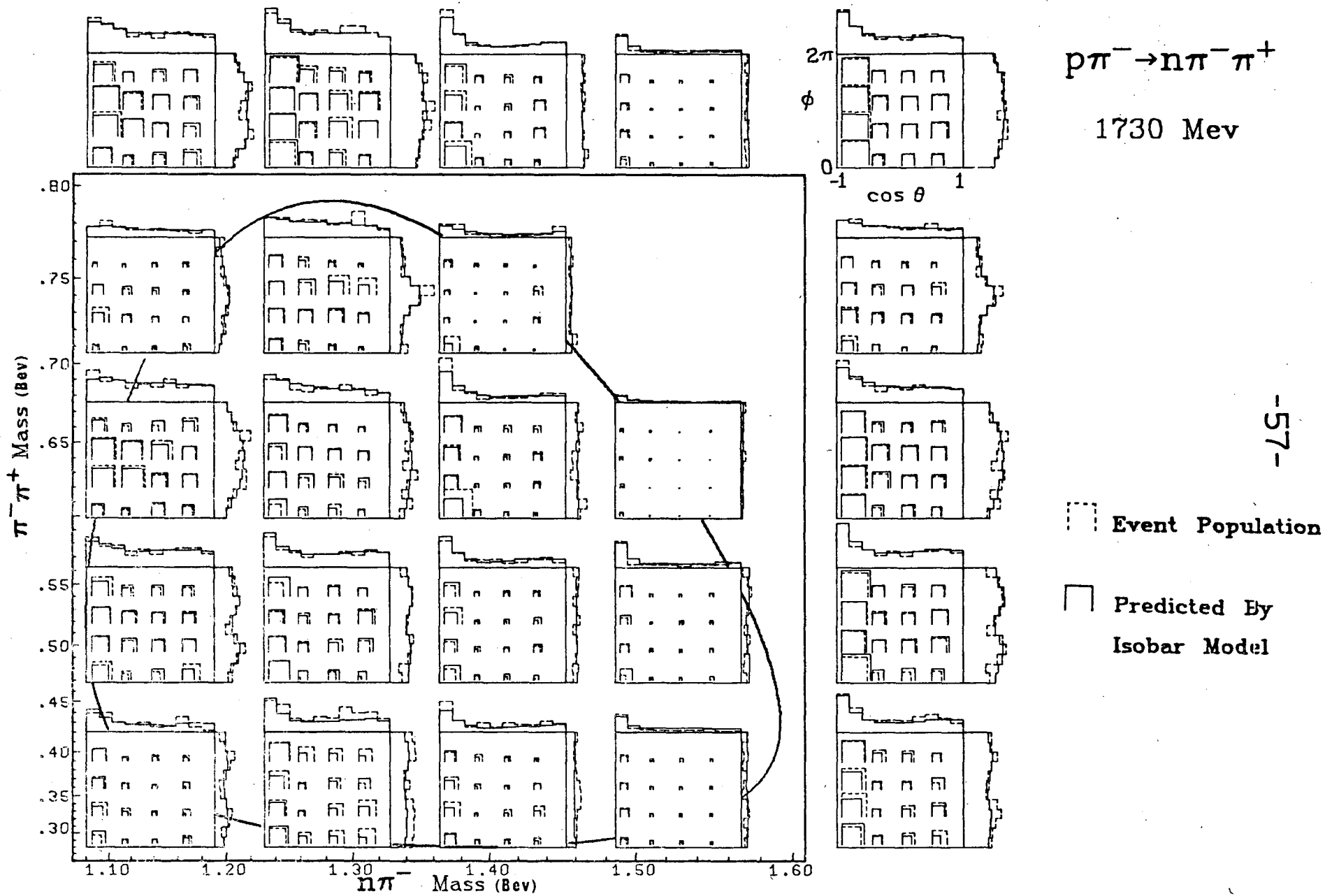


Fig. IIa Four-Dimensional Histogram

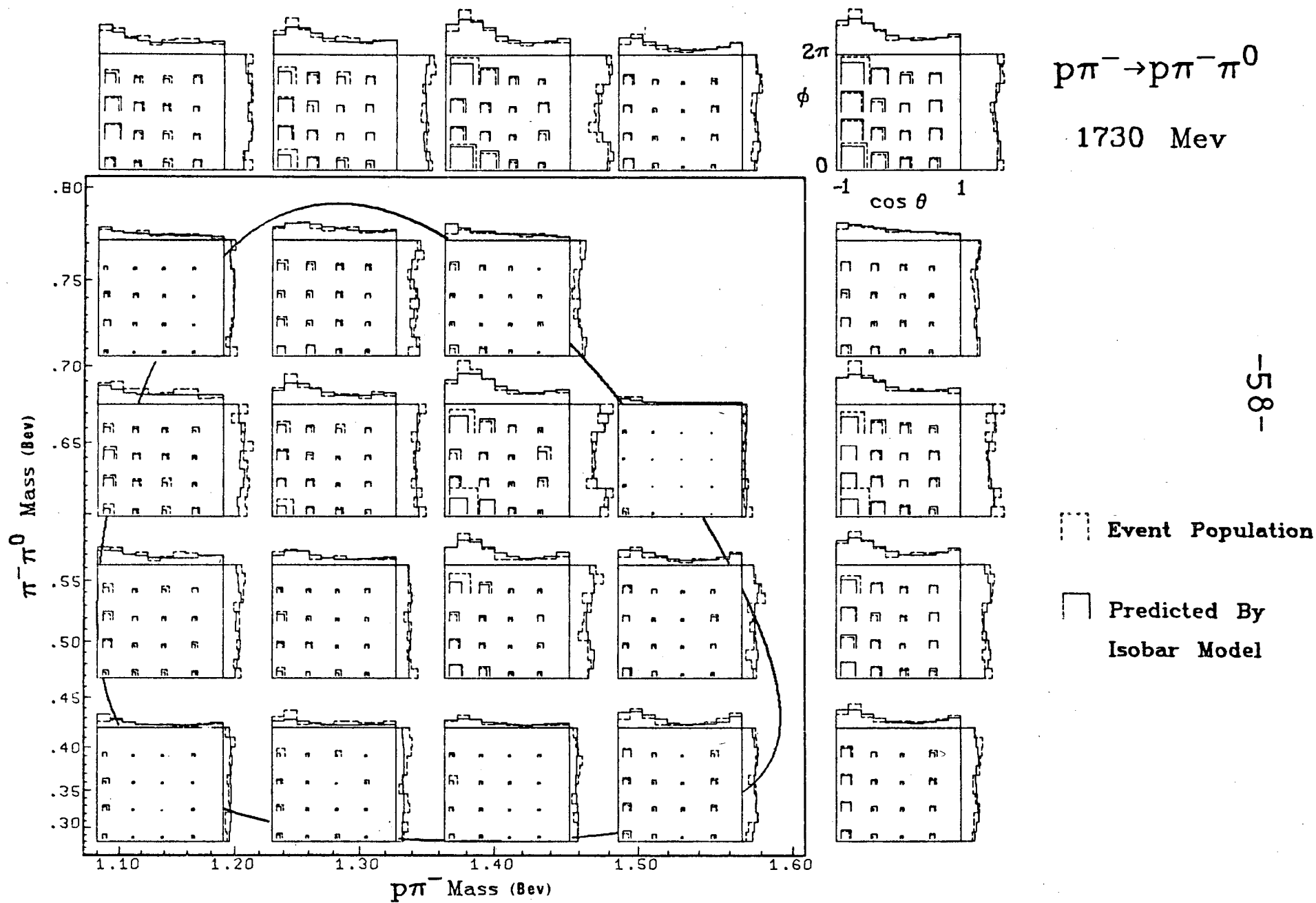


Fig. 11 b Four-Dimensional Histogram



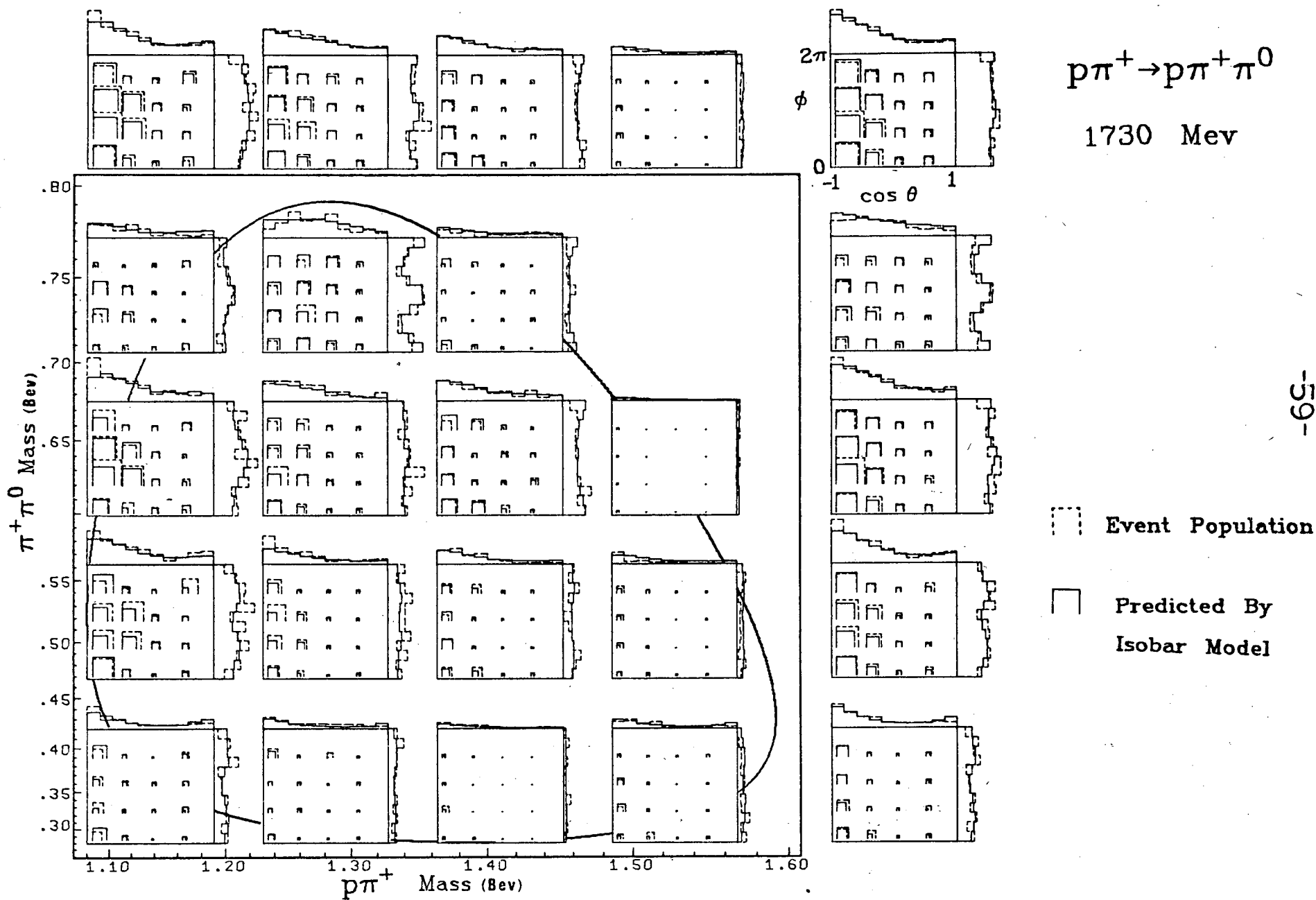


Fig. 11c Four-Dimensional Histogram

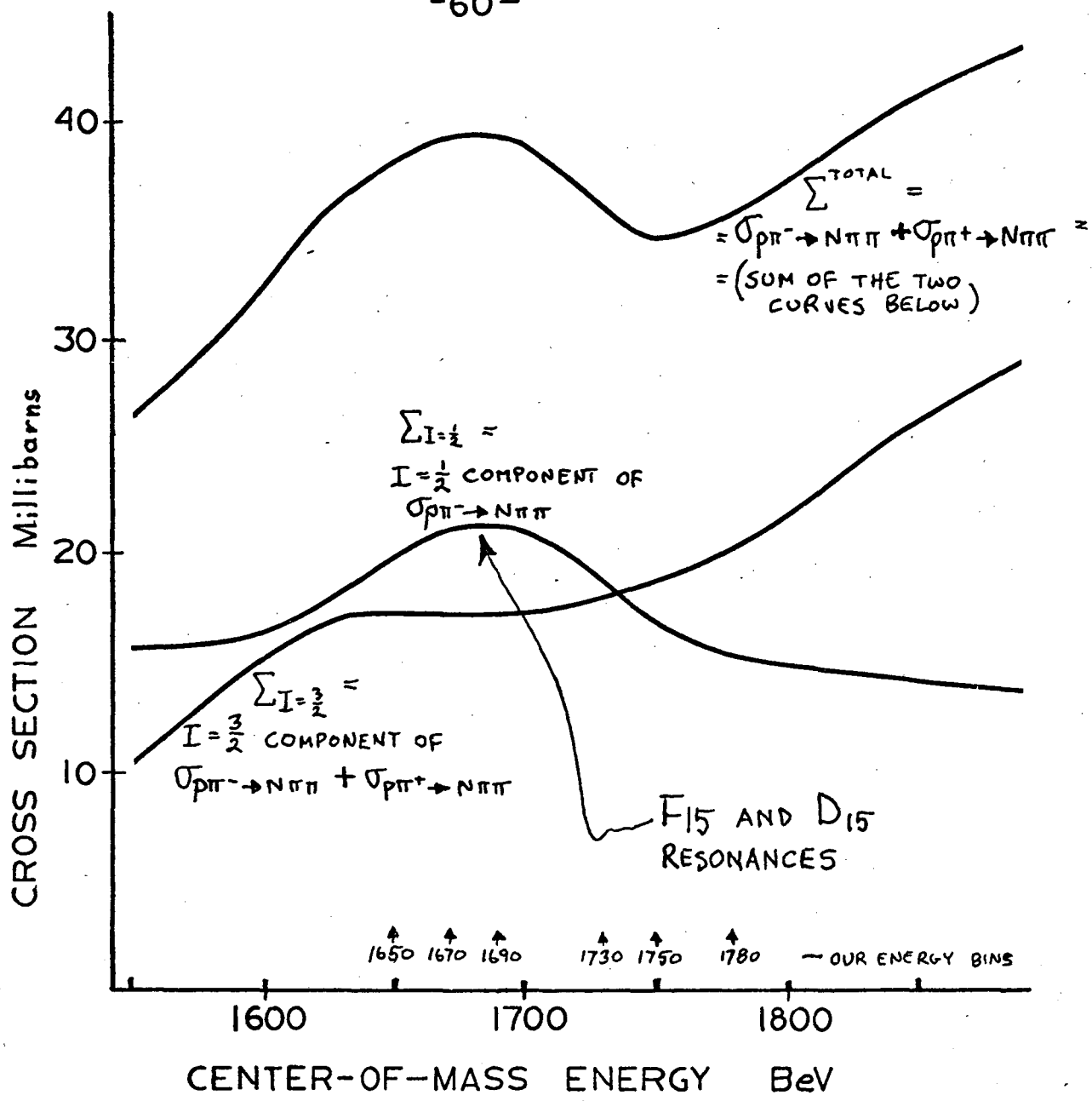


Fig. 12 Nπ INELASTIC CROSS SECTIONS

— Predicted From Elastic Partial Wave Analysis

• Predicted By Isobar Model

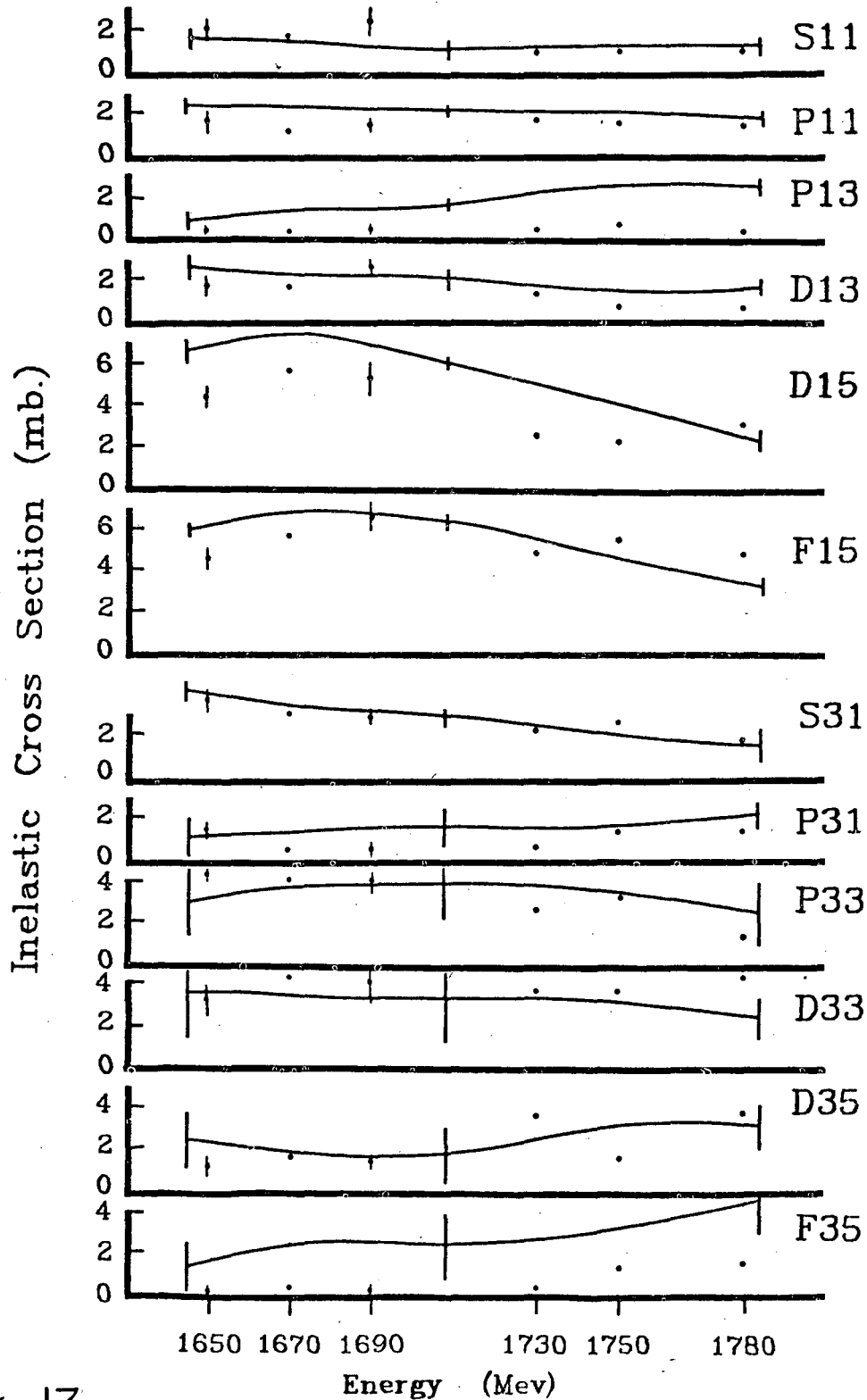
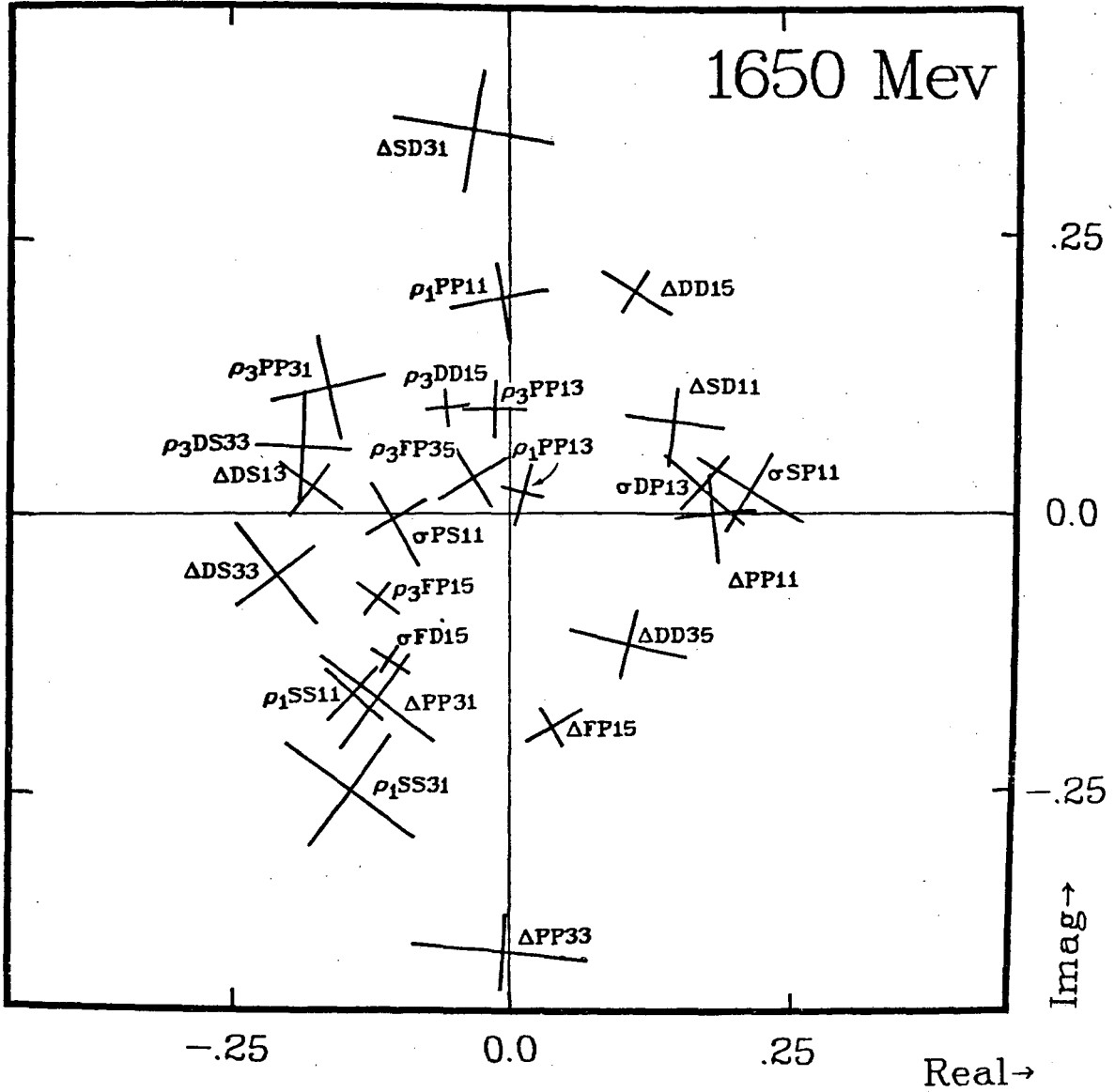


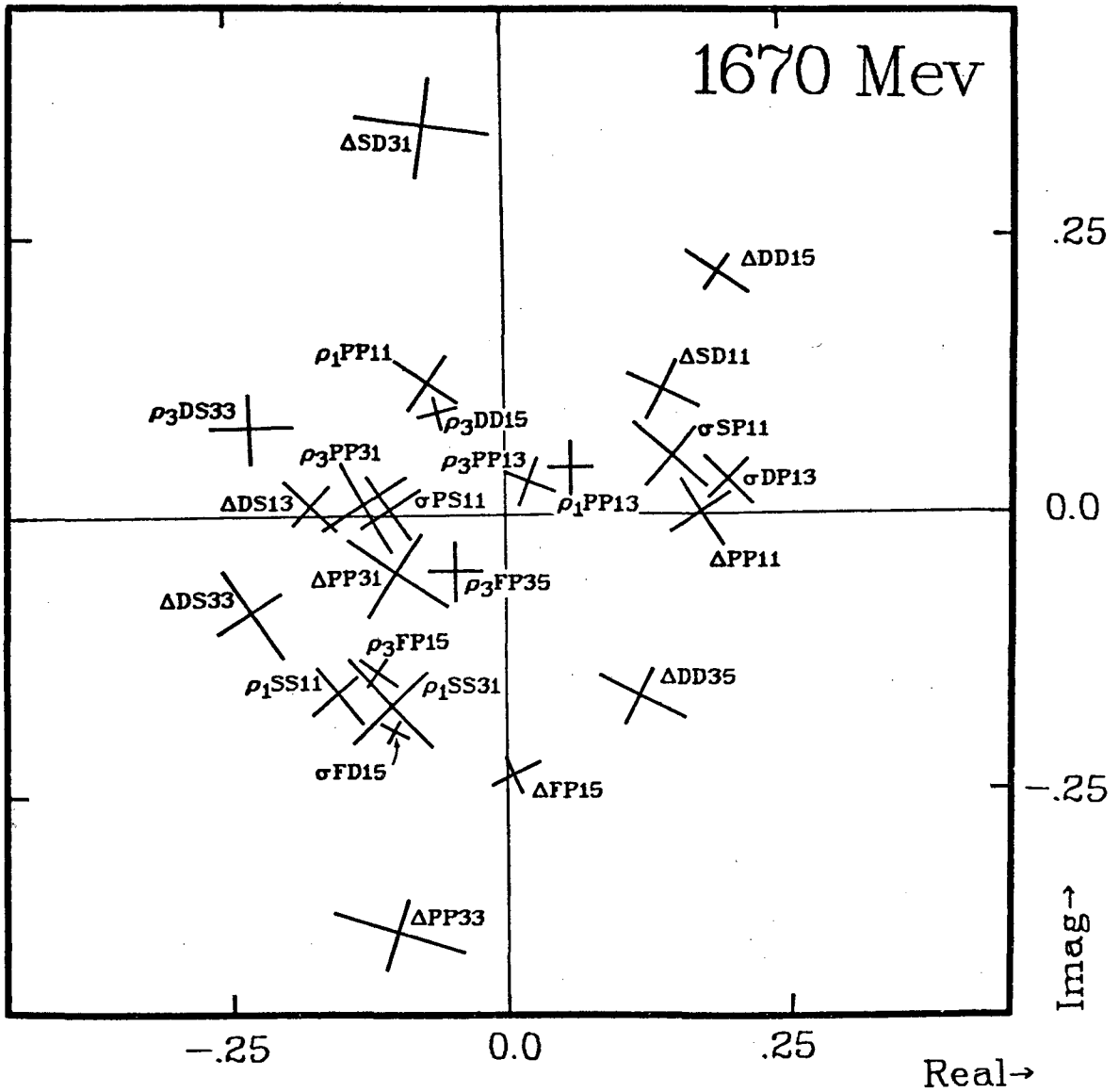
Fig. 13

Comparison of Partial-Wave Cross Sections



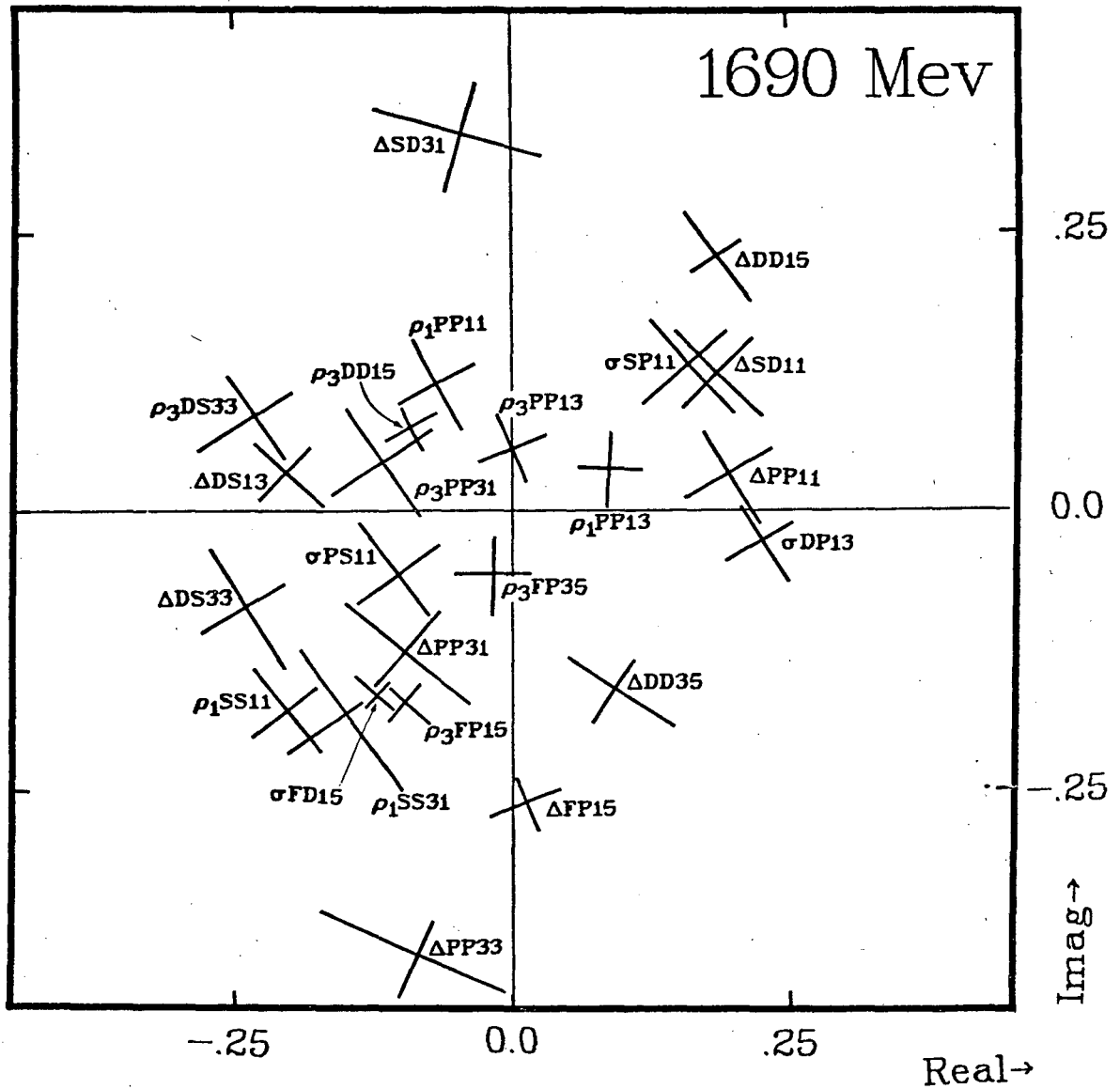
Error Bars are Major and Minor Axes of  $2\sigma$  Error Ellipse.

Fig 14a T-MATRIX ELEMENTS at 1650 MeV



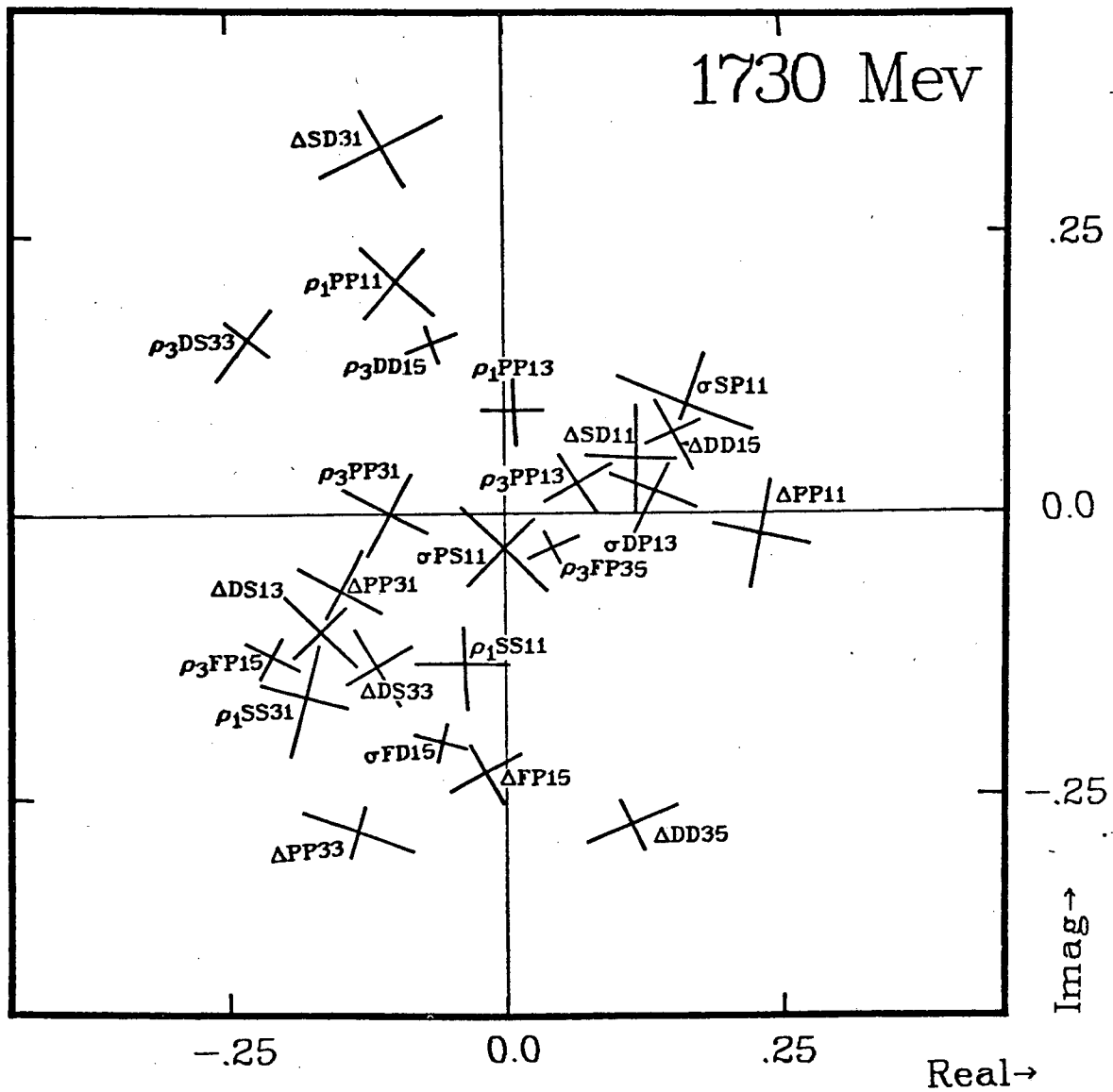
Error Bars are Major and Minor Axes of  $2\sigma$  Error Ellipse.

Fig 14b T-MATRIX ELEMENTS at 1670 MeV



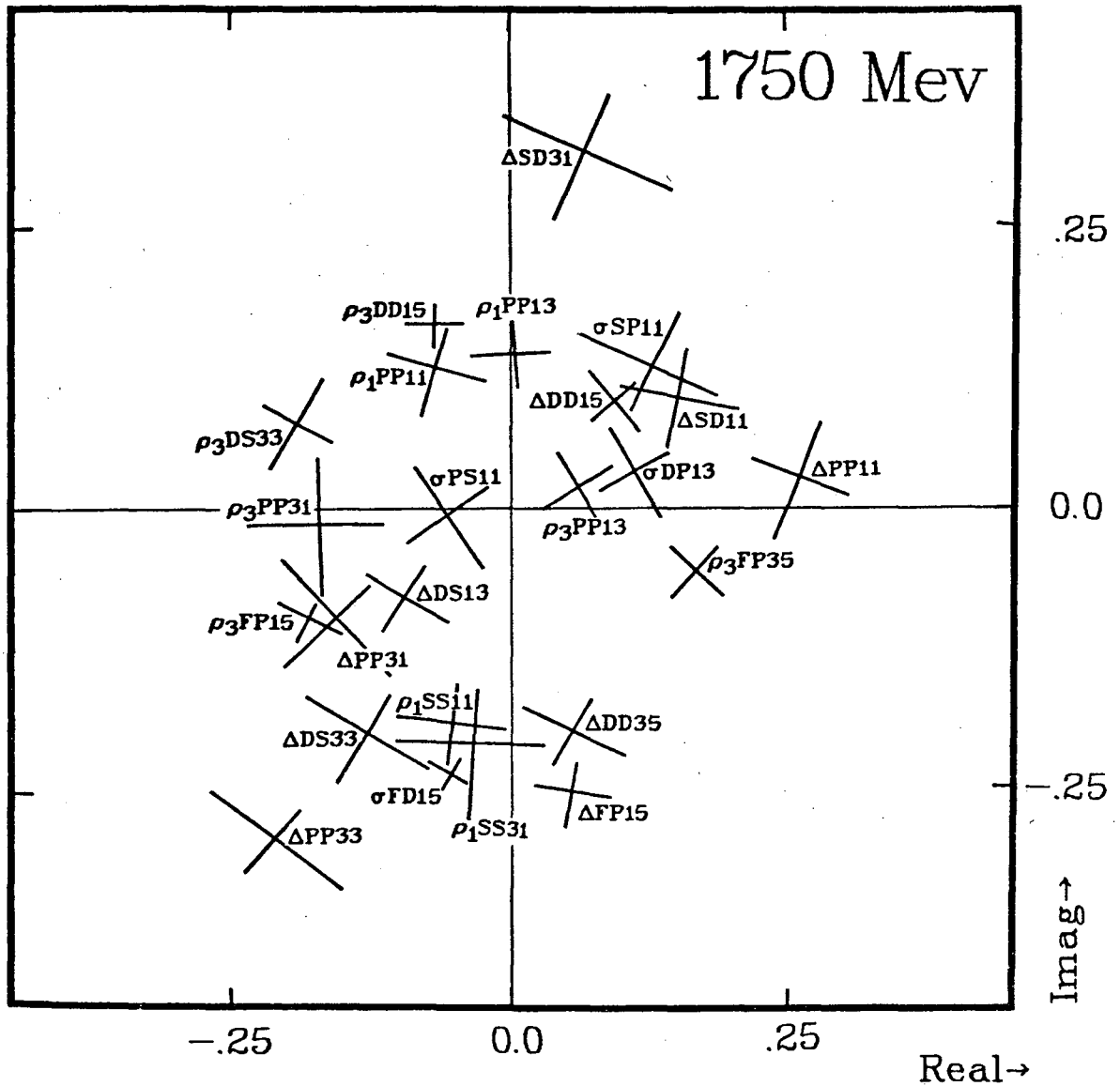
Error Bars are Major and Minor Axes of  $2\sigma$  Error Ellipse.

Fig 14c T-MATRIX ELEMENTS at 1690 MeV



Error Bars are Major and Minor Axes of  $2\sigma$  Error Ellipse.

Fig 14d T- MATRIX ELEMENTS at 1730 MeV



Error Bars are Major and Minor Axes of  $2\sigma$  Error Ellipse.

Fig 14e T- MATRIX ELEMENTS at 1750 MeV



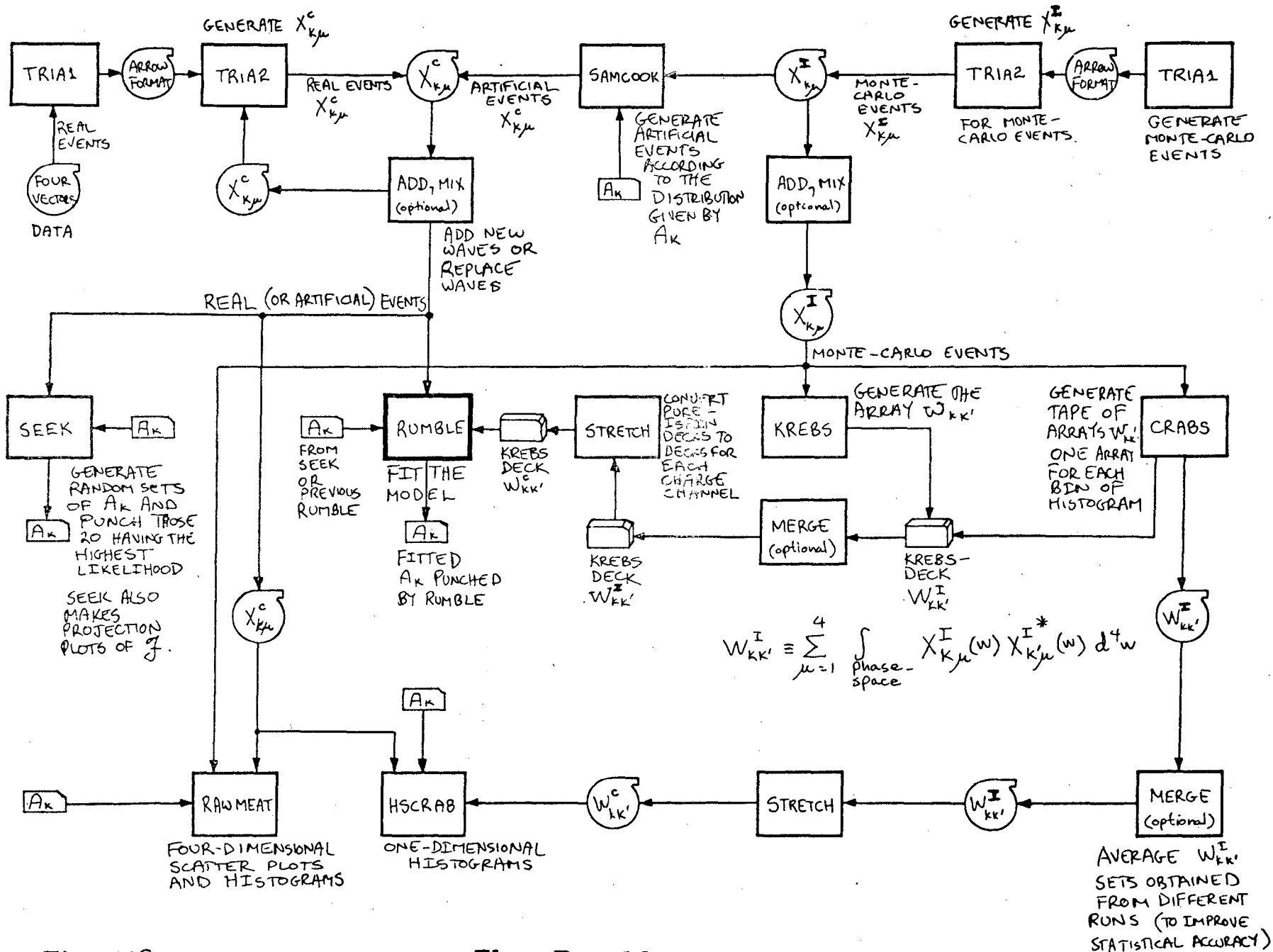


Fig. 16

The Rumble System

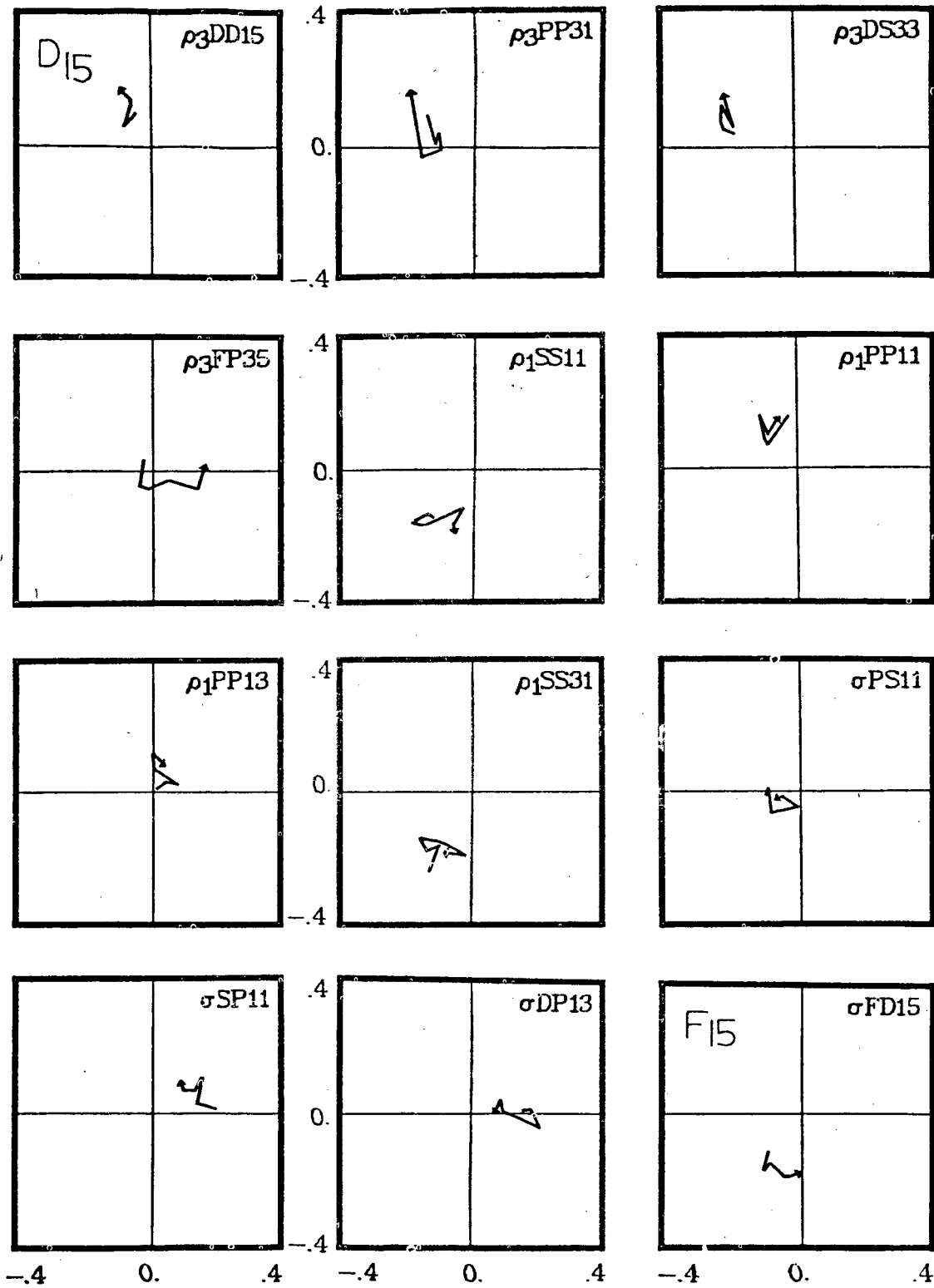


Fig. 15 (continued)

LEGAL NOTICE

*This report was prepared as an account of work sponsored by the United States Government. Neither the United States nor the United States Atomic Energy Commission, nor any of their employees, nor any of their contractors, subcontractors, or their employees, makes any warranty, express or implied, or assumes any legal liability or responsibility for the accuracy, completeness or usefulness of any information, apparatus, product or process disclosed, or represents that its use would not infringe privately owned rights.*

TECHNICAL INFORMATION DIVISION  
LAWRENCE BERKELEY LABORATORY  
UNIVERSITY OF CALIFORNIA  
BERKELEY, CALIFORNIA 94720